

Multidimensional Small Baseline Subset (MSBAS)

(no) theory processing manual

Sergey V. Samsonov, Senior Research Scientist

Canada Centre for Mapping and Earth Observation, Natural Resources Canada

580 Booth Street, Ottawa, ON, K1A 0E4, Canada

Email (work): sergey.samsonov@nrcan-rncan.gc.ca, Email (private): samsonov@insar.ca

Rational (typical scenario)

- Study ground deformation of a region over a substantial period of time
- SAR data from several satellites and orbits is available
- A large number (e.g., 10s, 100s, 1000s) of interferograms is produced
- How to analyze these interferograms? Two possibilities:
 - Manually analyze each interferogram – slow and tedious, especially if signal is small
 - Let software do the analyses and produce results that are easy to interpret – MSBAS way
- Familiar with Linux (Mac), GMT, GDAL also python tools, Gnuplot

What is MSBAS?

- Software written in C++ and designed to run on Linux computers
 - Can also run on Mac computers
- Computes from repeatedly acquired SAR-derived products
 - instantaneous deformation rate time series
 - cumulative deformation time series
 - linear deformation rates
- Does not assume any model
- Optional regularization produces smoothing in temporal domain
- Depending on input data and control flags produces deformation time series of dimension
 - 1D – line-of-sight
 - 2D – east and vertical
 - 3D-SPF – north, east and vertical, assuming Surface Parallel Flow constraint
 - 3D - north, east and vertical
 - 4D - north, east and vertical SPF and nSPF

Input data

- DInSAR - geocoded unwrapped interferograms in meters; negative values correspond to lengthening of line-of-sight (i.e., apparent subsidence)
- SPO-RO – speckle offsets in range direction in meters, same convention as DInSAR
- SPO-AO - speckle offsets in azimuth direction in meters, positive values correspond to displacements along the flight direction, ascending orbit ~ north, descending orbit ~ south
- DEM first central derivatives along the north and east directions
 - `gmt grdfilter dem.tif -D2 -Fg10 -fg -Gdem_flt.tif=gd+n0:Gtiff` (i.e., **10 km window**)
 - `gmt grdmath dem_flt.tif DDY 0 DENAN -M -fg = dem_flt_ns.tif=gd+n0:Gtiff`
 - `gmt grdmath dem_flt.tif DDX 0 DENAN -M -fg = dem_flt_ew.tif=gd+n0:Gtiff`
- All files are resampled to one grid
 - `gdalwarp -te lon1 lat1 lon2 lat2 -tr 0.001 0.001 -r average input.tif output.tif` or
 - `gdalwarp -te lon1 lat1 lon2 lat2 -ts 1000 1000 -r average input.tif output.tif`
 - Flags define te – window (in degrees), tr – resolution (in degrees), ts – number of samples

Solution dimension & input data

Table 1: Dimension of MSBAS time series is determined by type of input data and control flags. RO_{asc} , RO_{dsc} , AO_{asc} , AO_{dsc} are ascending and descending range and ascending and descending azimuth measurements. DInSAR and SPO-RO range measurements are considered equivalent. More than one set of similar type can be used. DD_NSEW_FILES are first central derivatives along north and east directions. D_FLAG is processing control flag. SPF is Surface-Parallel Flow constraint.

DInSAR == SPO-RO

No	MSBAS Technique	RO_{asc}	RO_{dsc}	AO_{asc}	AO_{dsc}	DD_NSEW_FILES	$D_FLAG = 1$
1	1D	×					
2	1D		×				
3	1D			×			
4	1D				×		
5	2D	×	×				
6	3D	×	×	×			
7	3D	×	×		×		
8	3D	×	×	×	×		
9	3D-SPF	×	×			×	
10	3D-SPF	×		×		×	
11	3D-SPF		×		×	×	
12	3D-SPF	×	×	×		×	
13	3D-SPF	×	×		×	×	
14	3D-SPF	×	×	×	×	×	
15	4D	×	×	×		×	×
16	4D	×	×		×	×	×
17	4D	×	×	×	×	×	×

MSBAS studies (see last slide)

Table 2: Studies that use MSBAS software for computing deformation time series.

Application	Technique	Region	Study(ies)
Mining - Coal	2D	France and Germany	13
Mining - Potash	2D	Saskatchewan, Canada	14, 15
Mining - Potash	1D, 2D	Perm Krai, Russia	16
Mining - Oil	1D	Alberta, Canada	17, 18
Subsidence	2D	Mexico City	4
Subsidence	2D	Seattle	19
Subsidence	2D	Vancouver	20
Cryosphere - Pingo	2D	NWT, Canada	21
Cryosphere - Glaciers	3D	British Columbia, Canada	22
Cryosphere - Glaciers	3D-SPF	Nunavut, Canada	23
Cryosphere - Glaciers	4D	British Columbia, Canada	24, 28
Hazards-Landslides	3D-SPF	Bukavu, DR Congo	25, 26, 27
Hazards-Landslides	1D, 2D	British Columbia, Canada	28
Hazards-Volcanoes	2D	various	29, 30, 31, 32, 33
CO ₂ sequestration	2D	Saskatchewan, Canada	34, 35, 36
Geothermal power	2D	Baja California, Mexico	37, 38
Natural gas storage	2D	California, USA	39
Others	2D	various	40, 41

Compile and run MSBAS

- Compile
 - git clone <https://github.com/insar-info/msbas>
 - cd msbas/src
 - make all
- Run
 - msbas param.txt
 - Content of param.txt

```
FORMAT=2, 3
FILE_SIZE=5146, 4777
C_FLAG=10
R_FLAG=2, 0.1
SET=0, 011547, -16.594721, 39.344300, MSBAS_049_0181_SET.txt, 049_0181/20230413_VV_lv_theta.geo.tif, 049_0181/20230413_VV_lv_phi.geo.tif
SET=0, 134555, 196.621960, 39.125200, MSBAS_071_0404_SET.txt, 071_0404/20211202_VV_lv_theta.geo.tif, 071_0404/20211202_VV_lv_phi.geo.tif
```

Processing control flags

Table 3: MSBAS processing control flags. Types are i - integer, f - float and s - string. Square brackets indicate that only one value is permitted (e.g. $[0, 1]$, either 0 or 1). Δr is interpolation radius. x and y are width and length of interferograms. x_a , x_b , y_a and y_b are first and last columns and rows of sub-region to be processed. x_i and y_i are column number and row number of reference region(s), up to nine regions are supported. Δx and Δy are half-width/length of reference region(s). λ is regularization parameter. *topo_grad_north* and *topo_grad_east* are first central derivatives along north and east directions. In SET, first parameter indicates DInSAR or SPO-RO (0) or SPO-AO (1) data. *hhmmss* is set's acquisition time (must be six digits). θ and ϕ are azimuth and incidence angles, measured in degrees. *lv_theta* and *lv_phi* are files with look vector elevation and orientation angles at each map pixel. Lines can be commented with # symbol.

Parameter	Type	Value(s)	Description
<i>FORMAT</i>	i	$[0, 1]$	4 bytes float small (0) or big (1) endian format
<i>FORMAT</i>	i, i	$2, \Delta r$	GeoTiff format, Δr - interpolation radius e.g. 1000, 1000
<i>FILE_SIZE</i>	i, i	x, y	default: 0, $x-1$, 0, $y-1$
<i>WINDOW_SIZE</i>	i, i, i, i	x_a, x_b, y_a, y_b	
<i>C_FLAG</i>	i	$[0, 10]$	no calibration (0) or zero average (10)
<i>C_FLAG</i>	i, i, i	$100, \Delta x, \Delta y$	minimal Z-score
<i>C_FLAG</i>	$i(s)$	$[1-9], x_1, y_1, x_2, y_2, \dots, \Delta x, \Delta y$	1-9 reference region(s)
<i>R_FLAG</i>	i	0	no regularization
<i>R_FLAG</i>	i, f	$[1, 2, 3], \lambda$	zeroth (1), first (2) or second (3) order regularization
<i>D_FLAG</i>	i	$[0, 1]$	MSBAS-3D (0) or MSBAS-4D (1)
<i>DD_NSEW_FILES</i>	s, s	<i>topo_grad_north</i> , <i>topo_grad_east</i>	e.g. <i>topo_grad_north.tif</i> , <i>topo_grad_east.tif</i>
<i>SET</i>	i, s, f, f, s	$[0, 1], hhmmss, \theta, \phi, set.txt$	e.g. 0, 122435, -189, 34, <i>dsc.txt</i> (DInSAR and RO (0) or AO (1))
<i>SET</i>	i, s, f, f, s, s, s	$[0, 1], hhmmss, \theta, \phi, set.txt, lv_theta, lv_phi$	e.g. 0, 122435, -189, 34, <i>dsc.txt</i> , <i>lv_theta.tif</i> , <i>lv_phi.tif</i>
#			comment

Processing control flag FORMAT

Defines format of input data (all files must be in the same format)

- FORMAT=0 – 4 bytes float small ending
- FORMAT=1 – 4 bytes float big ending
- FORMAT=2, 0 – GDAL library supported formats, GeoTiff (*.tif) is strongly recommended
 - 0 – do not fill gaps in data caused by decorrelation or other artefacts
- FORMAT=2, r
 - r – radius of window for filling gaps by interpolation
 - possible values 1-5, recommended values 2-3
- Converting data to geotif format
 - data2geotiff command (GAMMA)
 - gmt grdmath input.grd 1 MUL = output.tif=gd+n0:Gtiff (GMT)
- Example: FORMAT=2, 3

Processing control flag FILE_SIZE

Defines size of input and output files

- FILE_SIZE=x, y – x columns and y rows
- gmt grdinfo and gdalinfo display this information
- Example: FILE_SIZE=1000, 2000

Processing control flag WINDOW_SIZE

Limits processing to subregion, **optional** and **not recommended**

- Alternative recommended approach – subset region of interest with gdalwarp –te –tr
- `WINDOW_SIZE=x1, x2, y1, y2`
 - $x1, x2$ in range 0, $x-1$ and $y1, y2$ in range 0, $y-1$
- Example: `WINDOW_SIZE=0, 999, 0, 1999`

Processing control flag C_FLAG

Calibration against reference region(s)

- C_FLAG=0 – do not calibrate because data is externally calibrated
- C_FLAG=1, x1, y1, dx, dy – one reference region at x1,y1 of a radius dx,dy (≥ 0) **(Recommended)**
- C_FLAG=2, x1,y1, x2, y2, dx, dy – two reference regions at x1,y1 and x2,y2 of a radius dx,dy (≥ 0)
- C_FLAG=9, ... - up to nine reference regions supported
- C_FLAG=10 – zero average of entire region **(Good first choice)**
- C_FLAG=100, dx, dy – reference region corresponds to minimal Z-score **(Recommended)**
- Example: C_FLAG=1, 500, 1500, 16, 16

Processing control flag R_FLAG

Tikhonov Regularization

- Manifests as temporal smoothing
- R_FLAG=0 – no regularization – can be noisy, still sometimes useful
- R_FLAG=1, λ – zeroth-order regularization
 - minimizes instantaneous displacement rates – usually underestimates solution
 - λ – regularization parameter, recommended values are in range 0.01-0.1, try and see, **do not overthink**
- R_FLAG=2, λ – first-order regularization
 - minimizes differences of consecutive deformation rates (**Recommended**)
- R_FLAG=3, λ – second-order regularization
 - Results are usually indistinguishable from the previous scenario
- Example: R_FLAG=2, 0.1

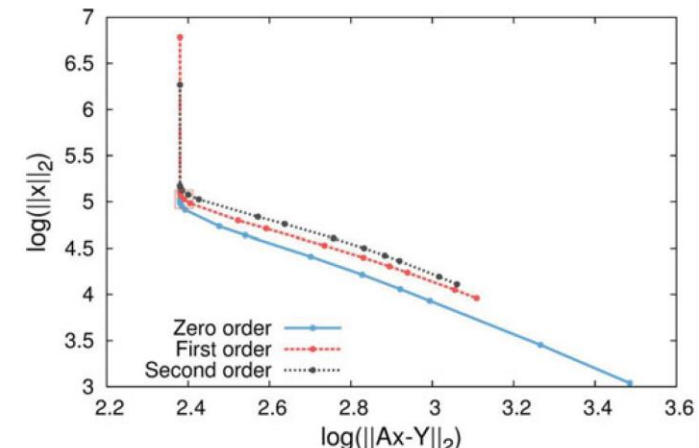


Figure 6. L-curve for zero, first, and second order regularizations for λ values in range 0.00001–1.0. Optimal value of 0.03 (marked) for first order regularization is used in this study.

Processing control flag SET

Defines dataset

- Dataset is collection of interferograms of similar geometry (incidence and azimuth angles and acquisition time)
- DInSAR and SPO-RO can be combined in one or two sets
- SET=0, hhmmss, azimuth, incidence, set.txt
 - 0 – DInSAR or SPO-RO, 1 – SPO-AO
 - hhmmss – acquisition time, same for all interferograms of specific set
 - azimuth angle in degrees
 - incidence angle in degrees
- SET=0, hhmmss, azimuth, incidence, set.txt, lv_theta.tif, lv_phi.tif (**More accurate**)
 - lv_theta.tif, lv_phi.tif – look vector elevation and orientation angles
 - Computed with GAMMA look_vector and data2geotiff commands

Processing control flag DD_NSEW_FILES

Defines first central derivatives along the north and east directions

- Required for 3D-SPF and 4D
- Recall
 - gmt grdfilter dem.tif -D2 -Fg**10** -fg -Gdem_flt.tif=gd+n0:Gtiff (i.e., **10 km window**)
 - gmt grdmath dem_flt.tif DDY 0 DENAN -M -fg = dem_flt_ns.tif=gd+n0:Gtiff
 - gmt grdmath dem_flt.tif DDX 0 DENAN -M -fg = dem_flt_ew.tif=gd+n0:Gtiff
- North then east
- Example: DD_NSEW_FILES=topo_grad_north.tif, topo_grad_east.tif

Processing control flag D_FLAG

If DD_NSEW_FILES defined = two possible solutions

- D_FLAG=0 – 3D-SPF
- D_FLAG=1 – 4D

Parameter file example (1D case)

```
FORMAT=2, 3
FILE_SIZE=6475, 4778
R_FLAG=2, 0.10
C_FLAG=100, 32, 32
SET=0, 011547, -16.594721, 39.344300, MSBAS_049_0181_SET.txt, 049_0181/20230413_VV_lv_theta.geo.tif,
049_0181/20230413_VV_lv_phi.geo.tif
```

Example of MSBAS_049_0181_SET.txt

```
049_0181/20170327_VV_20170408_VV.disp.geo.tif -114.0297 20170327 20170408
049_0181/20170408_VV_20170526_VV.disp.geo.tif 100.0671 20170408 20170526
049_0181/20170526_VV_20170619_VV.disp.geo.tif -89.135 20170526 20170619
049_0181/20170619_VV_20170701_VV.disp.geo.tif 6.5902 20170619 20170701
049_0181/20170701_VV_20170725_VV.disp.geo.tif 80.6455 20170701 20170725
```

...

- path to interferogram file
- perpendicular baseline in meters (not used and can be any number)
- acquisition date of earlier image in YYYYMMDD format
- acquisition date of later image in YYYYMMDD format

Example of parameter file (2D case)

```
FORMAT=2, 3
FILE_SIZE=5146, 4777
C_FLAG=10
R_FLAG=2, 0.1
SET=0, 011547, -16.594721, 39.344300, MSBAS_049_0181_SET.txt, 049_0181/20230413_VV_lv_theta.geo.tif,
049_0181/20230413_VV_lv_phi.geo.tif
SET=0, 134555, 196.621960, 39.125200, MSBAS_071_0404_SET.txt, 071_0404/20211202_VV_lv_theta.geo.tif,
071_0404/20211202_VV_lv_phi.geo.tif
```

MSBAS version 10 – partially coherent pixels

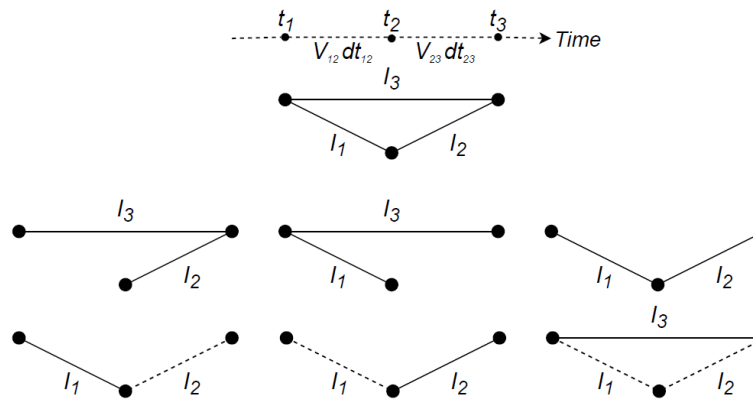
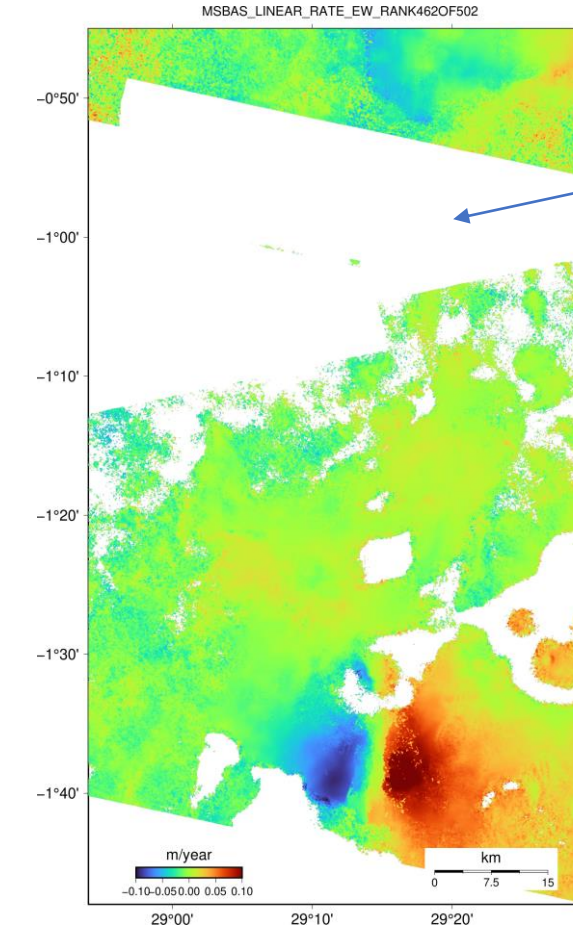
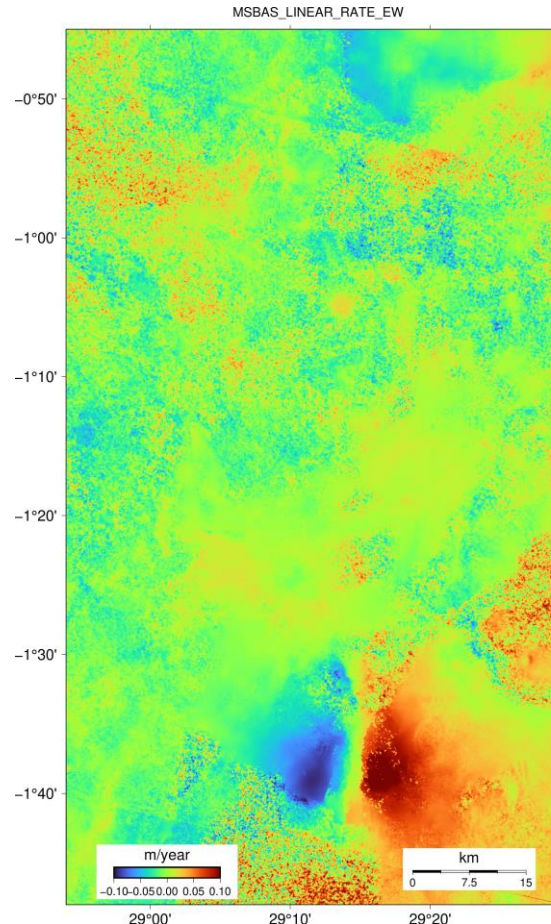
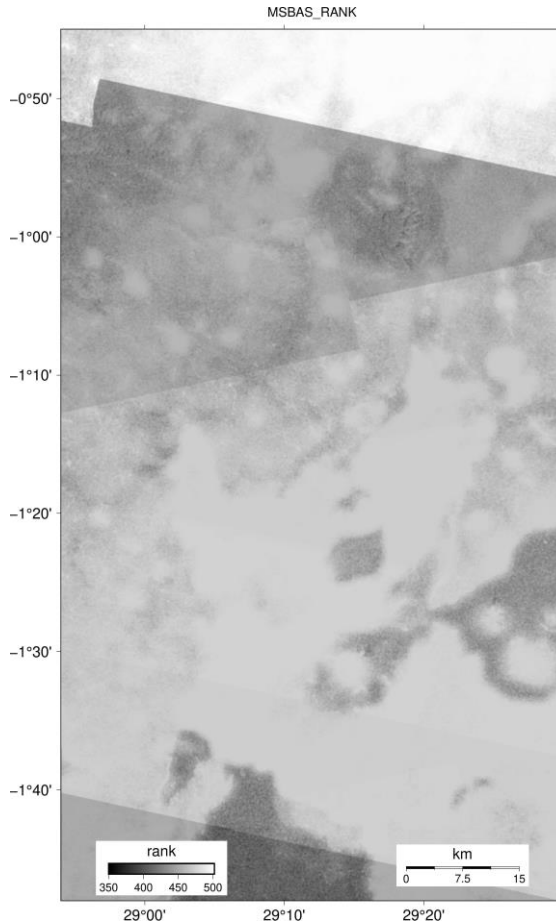


Figure 2: Schematics for estimating rank of time matrix for scenario with three SAR images (points) and three interferograms (lines). First, second and third rows make overdetermined, well-posed and underdetermined systems of equations, respectively. In all of these cases, MSBAS produces valid pixels in computed deformation time series and rates.

MSBAS version 10 – MSBAS_RANK

Removing pixels of very small rank with gdal_calc.py



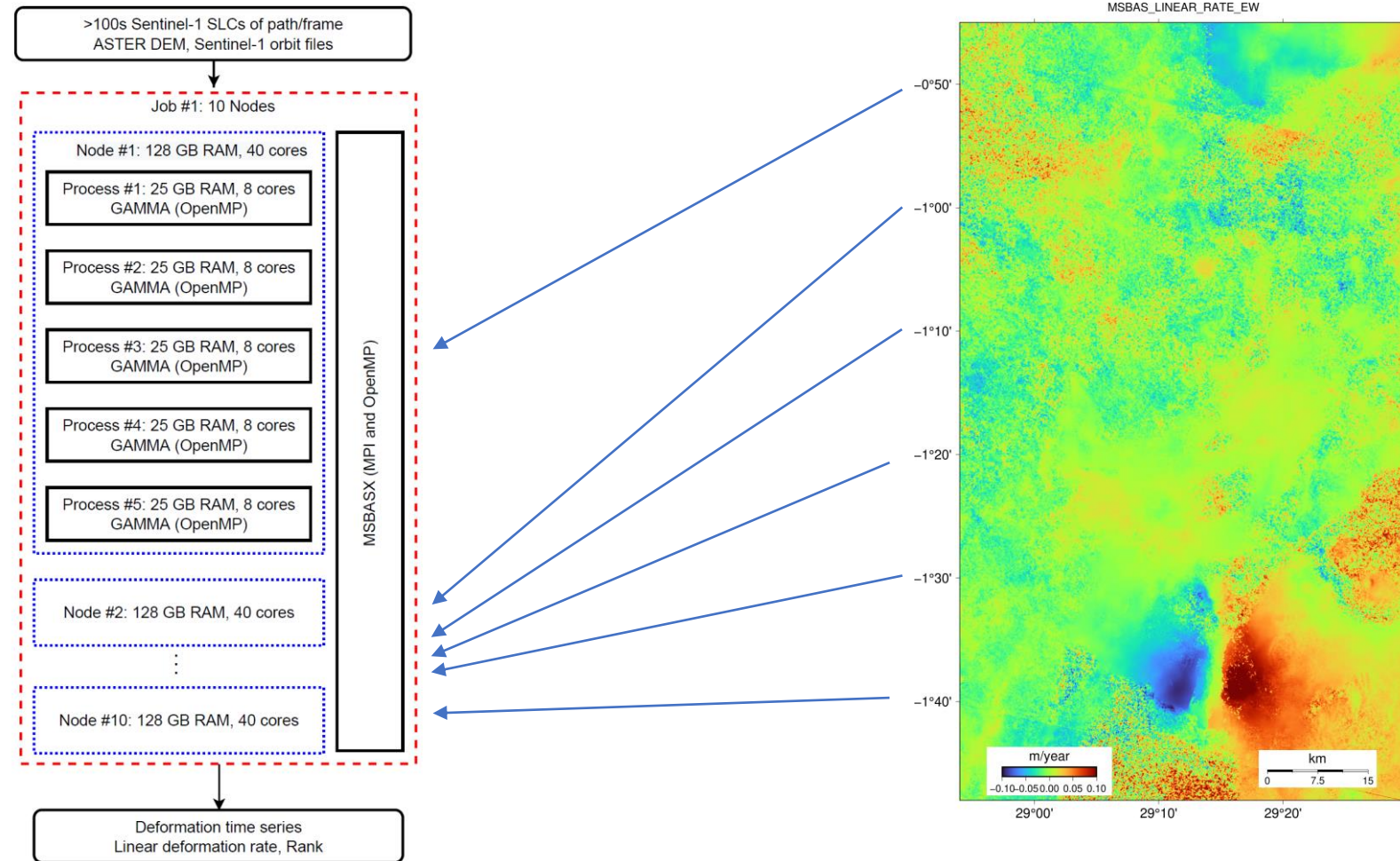
Data acquisition gap

gdal_calc.py -A MSBAS_LINEAR_RATE_EW.tif -R ~~MSBAS.rank~~ -calc="A*(R>=462)" -NoDataValue 0 -outfile MSBAS_LINEAR_RATE_EW_RANK462OF502.tif

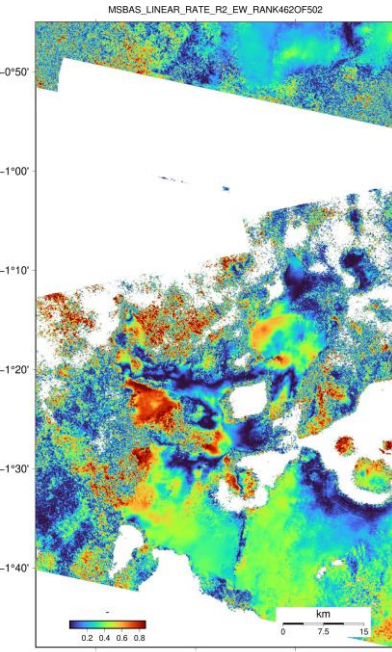
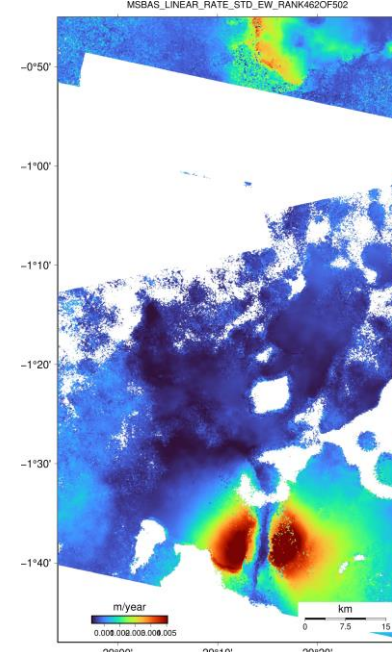
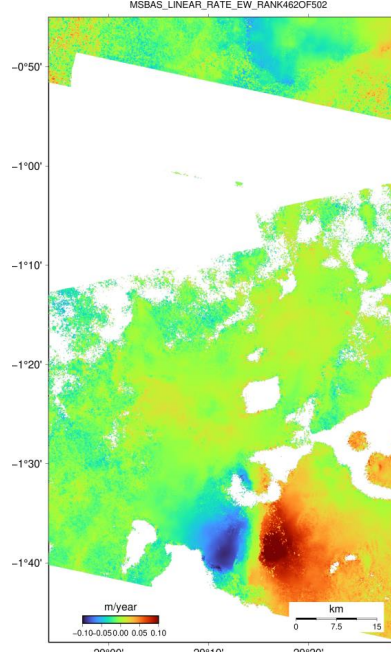
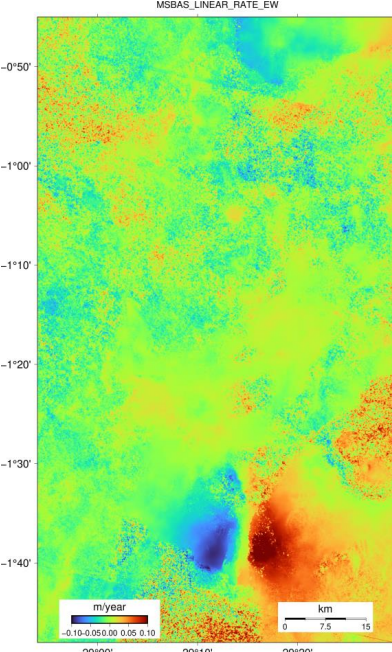
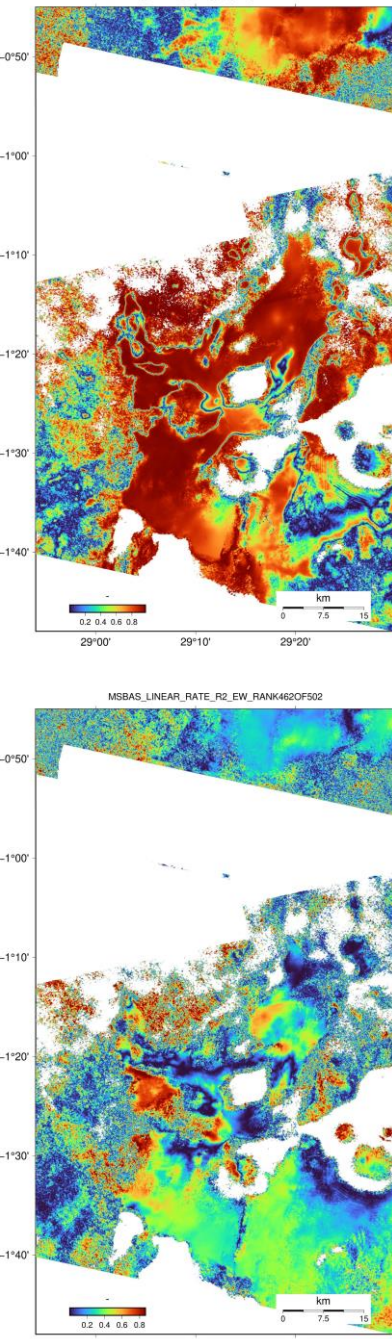
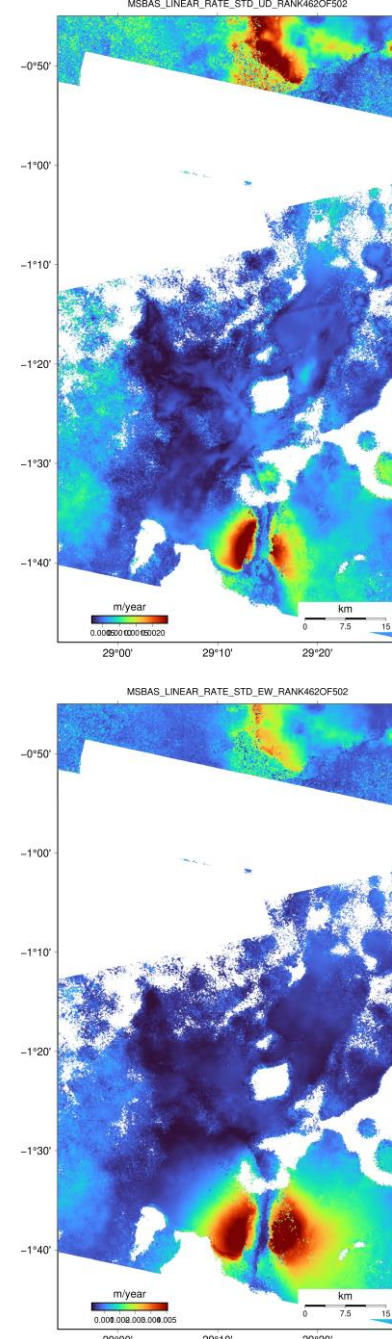
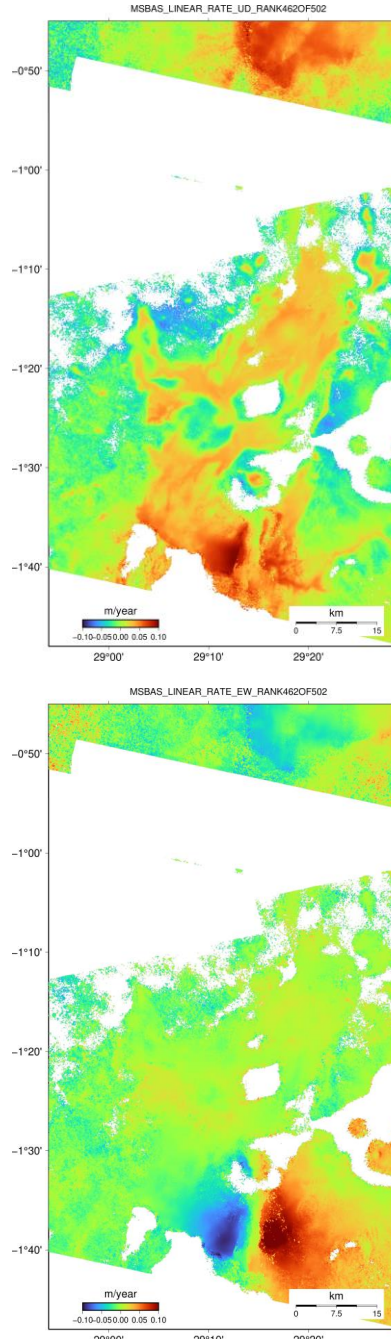
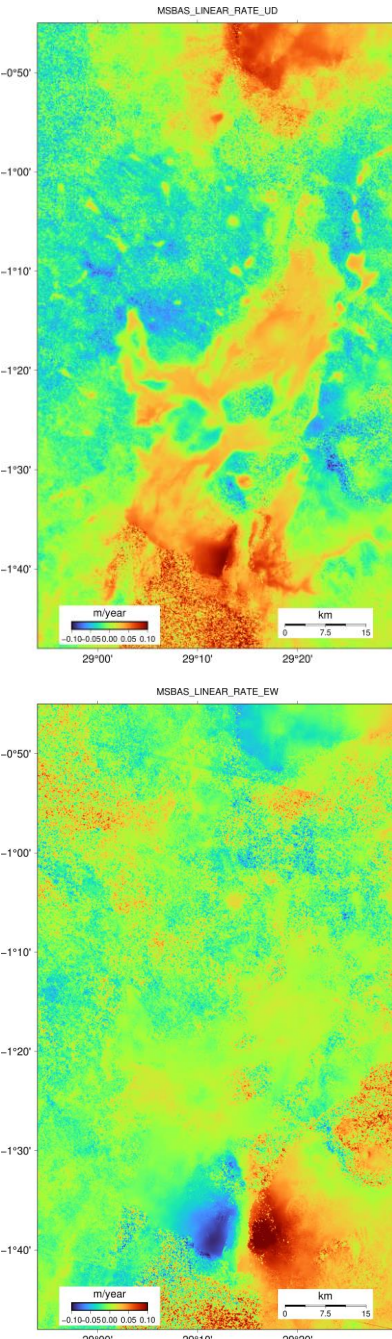
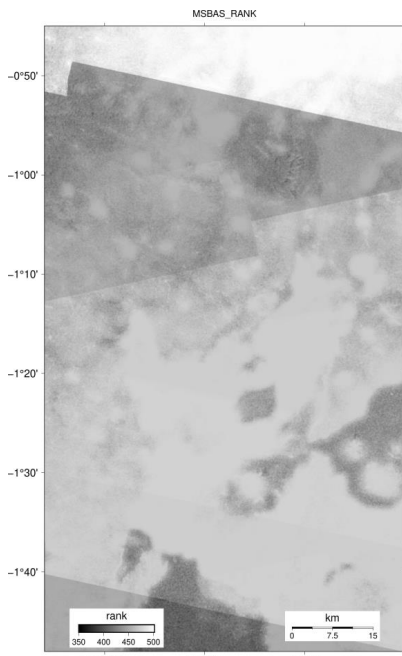
462 - mean value of MSBAS_RANK.tif and 502 - max value, try different

MSBAS version 10 – parallelization with MPI

- Distribute processing between different nodes
- Still very slow
- Want fast – use previous MSBAS versions



Output files



- Time series do not assume any model
- Linear dates assume linear model
- More complex models can be applied to time series directly

Output files (cont.)

These files (their average values) can be used for L-curve test

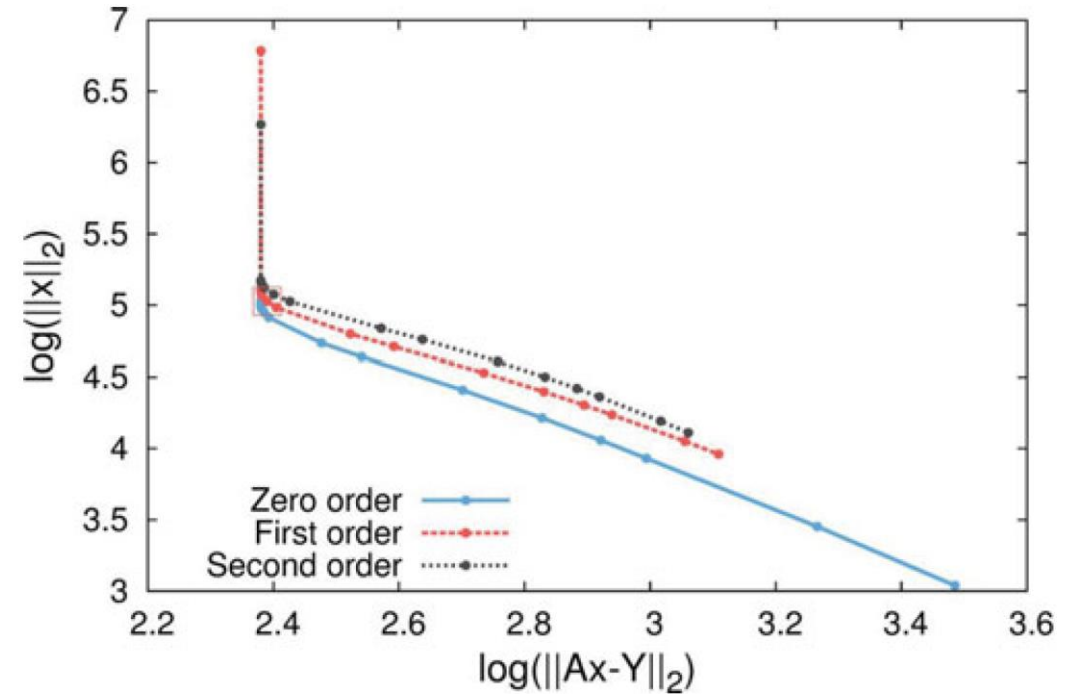
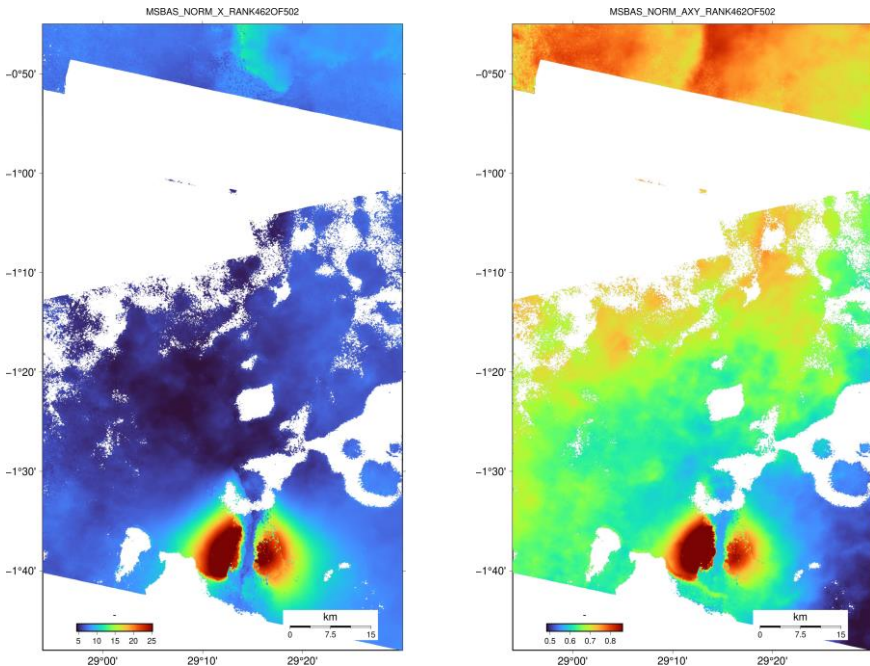


Figure 6. L-curve for zero, first, and second order regularizations for λ values in range 0.00001–1.0. Optimal value of 0.03 (marked) for first order regularization is used in this study.

Output files (cont.)

- MSBAS_TSOUT.txt – used for extracting and plotting cumulative deformation time series

FORMAT=2,1

FILE_SIZE=1550,2713

C_FLAG=10

20141017T162120 2014.793648 MSBAS_20141017T162120_EW.tif MSBAS_20141017T162120_UD.tif

20141031T034538 2014.830566 MSBAS_20141031T034538_EW.tif MSBAS_20141031T034538_UD.tif

20141110T162120 2014.859401 MSBAS_20141110T162120_EW.tif MSBAS_20141110T162120_UD.tif

20141124T034538 2014.896320 MSBAS_20141124T034538_EW.tif MSBAS_20141124T034538_UD.tif

...

- MSBAS_vTSOUT.txt – used for extracting and plotting deformation rate time series

FORMAT=2,1

FILE_SIZE=1550,2713

C_FLAG=10

20141017T162120 2014.793648 MSBAS_20141017T162120_vEW.tif MSBAS_20141017T162120_vUD.tif

20141031T034538 2014.830566 MSBAS_20141031T034538_vEW.tif MSBAS_20141031T034538_vUD.tif

20141110T162120 2014.859401 MSBAS_20141110T162120_vEW.tif MSBAS_20141110T162120_vUD.tif

20141124T034538 2014.896320 MSBAS_20141124T034538_vEW.tif MSBAS_20141124T034538_vUD.tif

...

Output files (cont.)

- MSBAS_LOG.txt – saves screen output

hello & welcome to msbasx

MPI process 0 of 10 with 40 OpenMP cores on host ib13be-028.science.gc.ca

...

MPI process 9 of 10 with 40 OpenMP cores on host ib13be-037.science.gc.ca

executing init by process 0 of 10

provided parameters:

FORMAT=2,1

FILE_SIZE=1550,2713

C_FLAG=100,32,32

R_FLAG=2,0.05

SET=0,034538,192.037133,39.574800,MSBAS_021_0593_0594_0595_0596_0597_0598_0599_SET.txt,021_0593_0594_0595_0596_0597_0598_0599/20220802_VV_lv_theta.geo.tif,021_0593_0594_0595_0596_0597_0598_0599/20220802_VV_lv_phi.geo.tif

0: 021_0593_0594_0595_0596_0597_0598_0599/20141007_VV_20141031_VV_disp.geo.tif -52.263 20141007 20141031

1: 021_0593_0594_0595_0596_0597_0598_0599/20141031_VV_20141124_VV_disp.geo.tif 133.5382 20141031 20141124

...

completed by process 7 of 10 100% on Sat Sep 3 18:30:48 2022

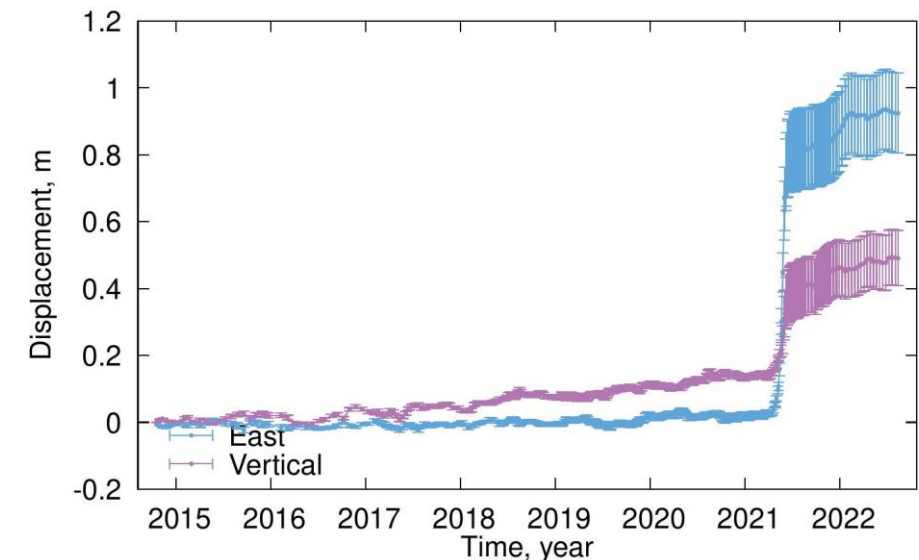
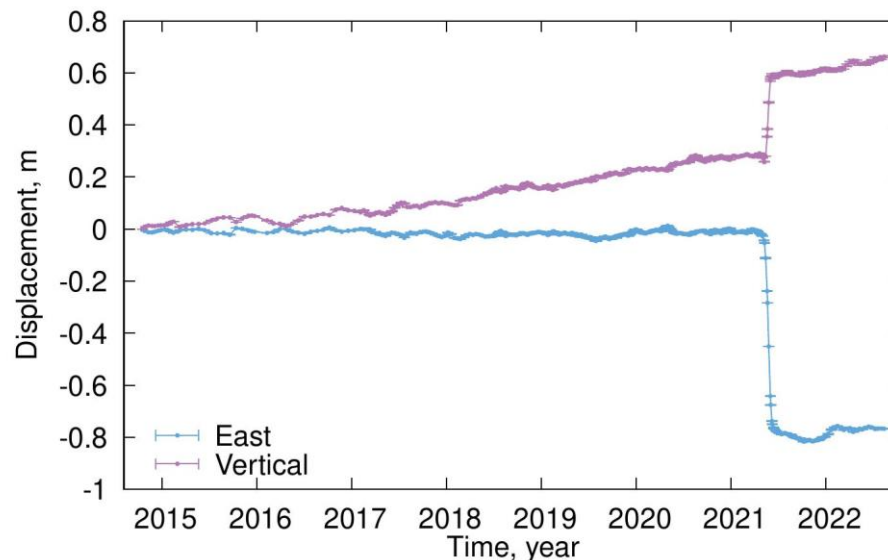
...

executing write by process 9 of 10

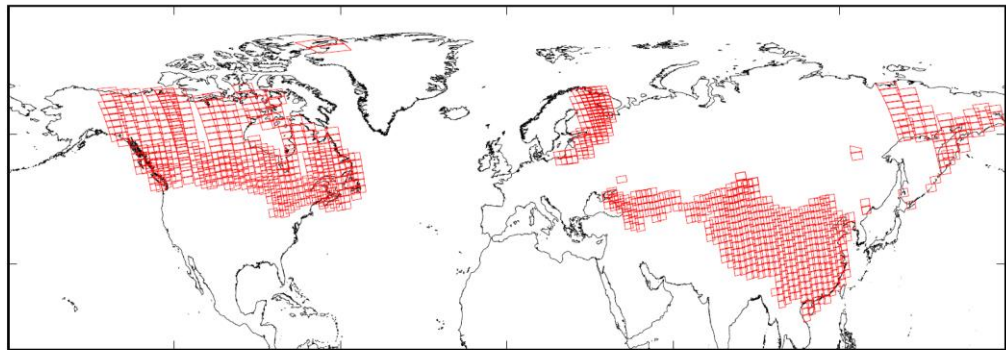
good bye

Additional tools

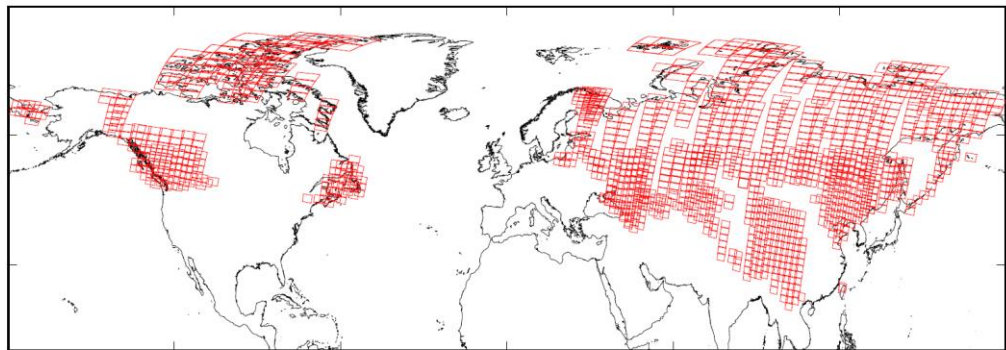
- `msbas_extract MSBAS_TSOUT.txt x y dx dy`
 - x, y – column and row of pixel
 - dx, dy – window size (2,2 creates 5x5=25-pixel region)
 - Produces `MSBAS_EXTRACT_x_y_dx_dy.txt` file
- `msbas_plot_ts.sh MSBAS_EXTRACT_x_y_dx_dy.txt`
 - Plots time series
 - Requires gnuplot



Recent and unpublished results, 2200 K Sentinel-1 frames

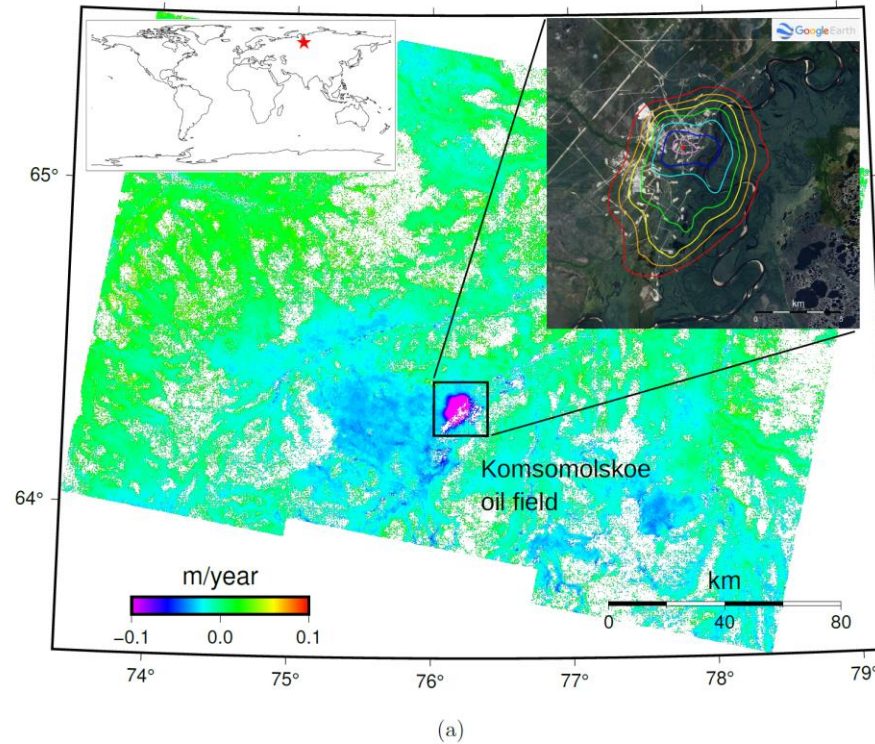


(a)

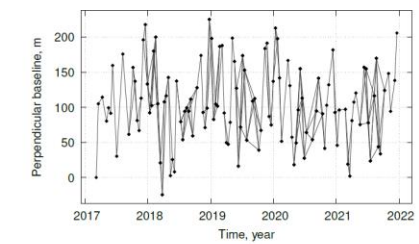


(b)

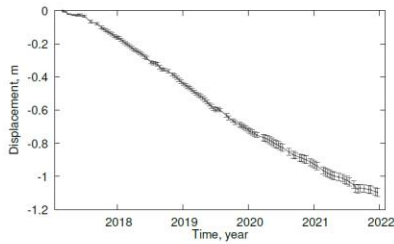
Figure 3: Spatial coverage of Sentinel-1 ascending (a) and descending (b) SAR frames with over hundred SLC images per frame used in this study.



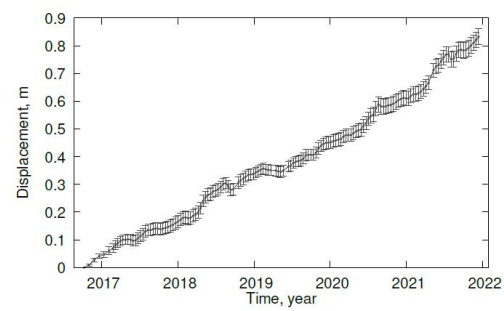
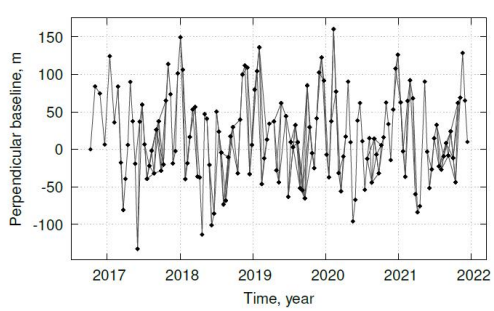
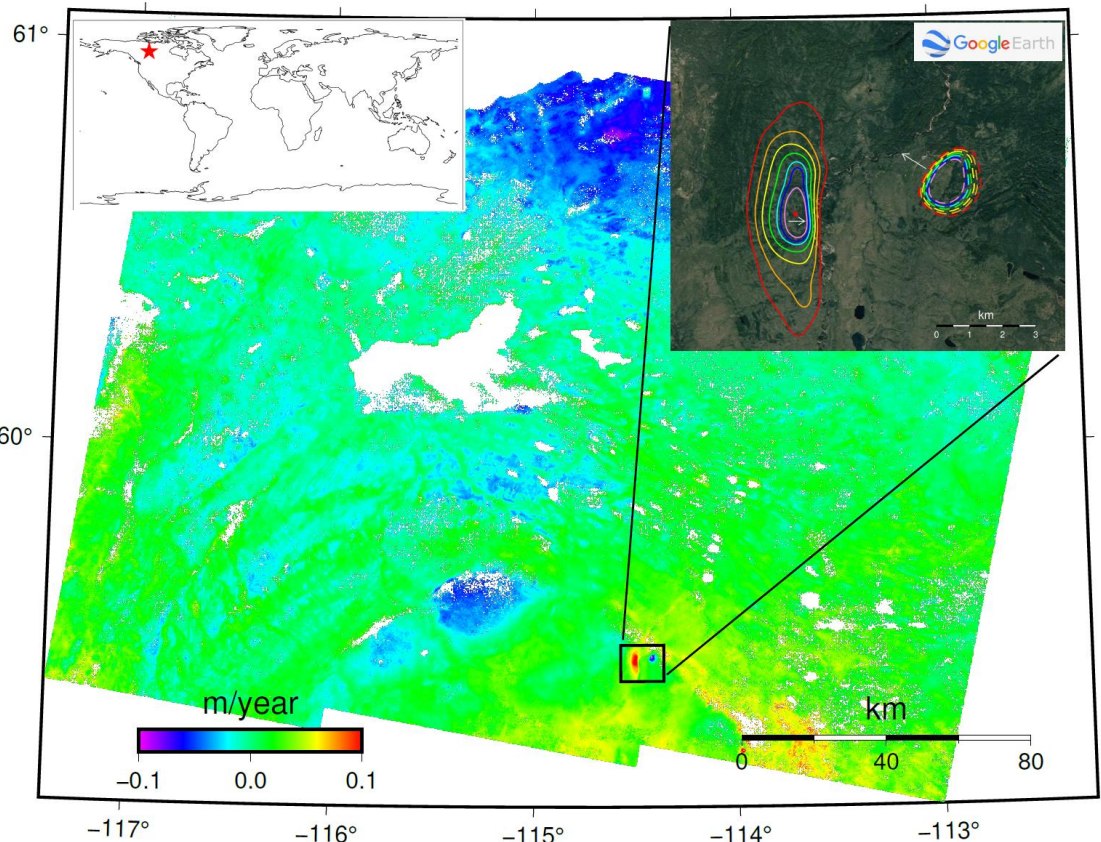
(a)



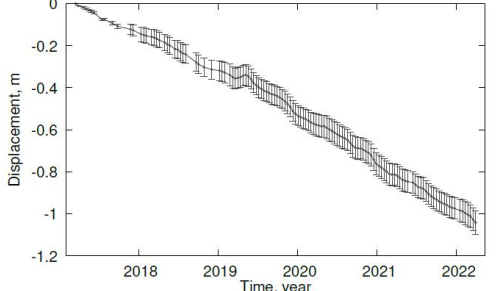
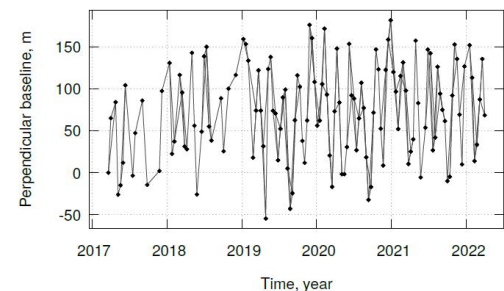
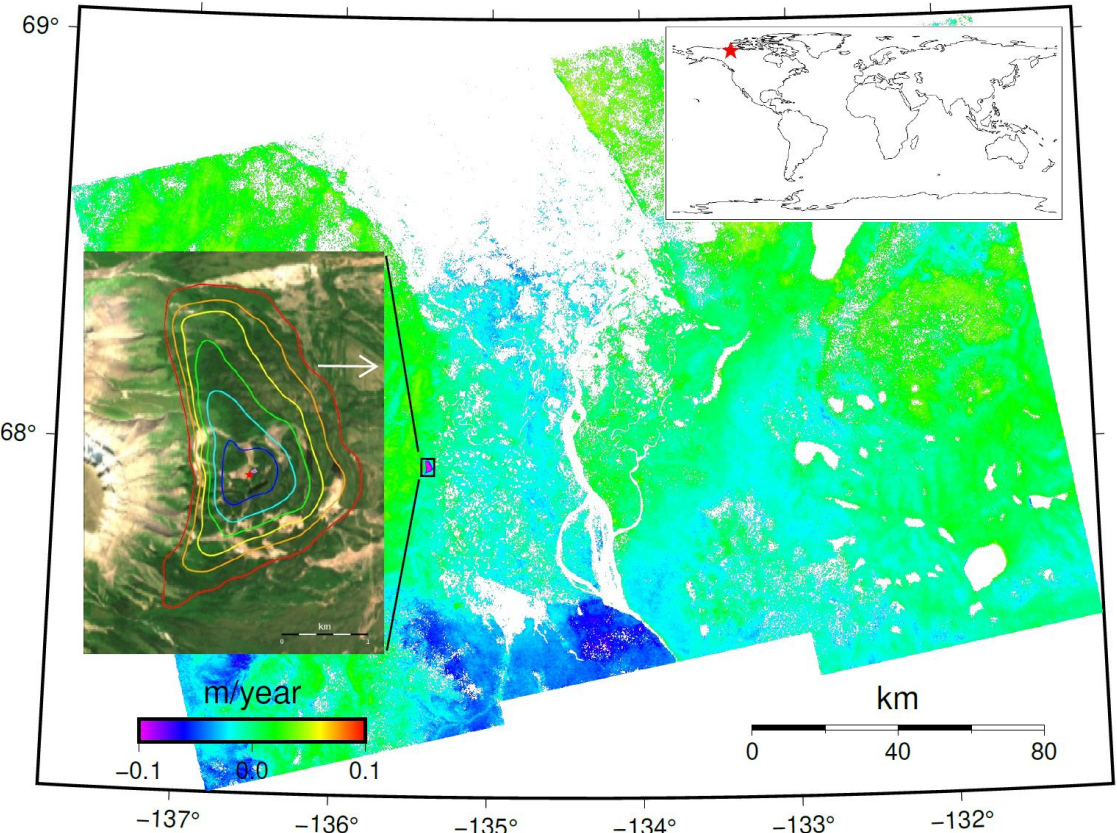
(b)

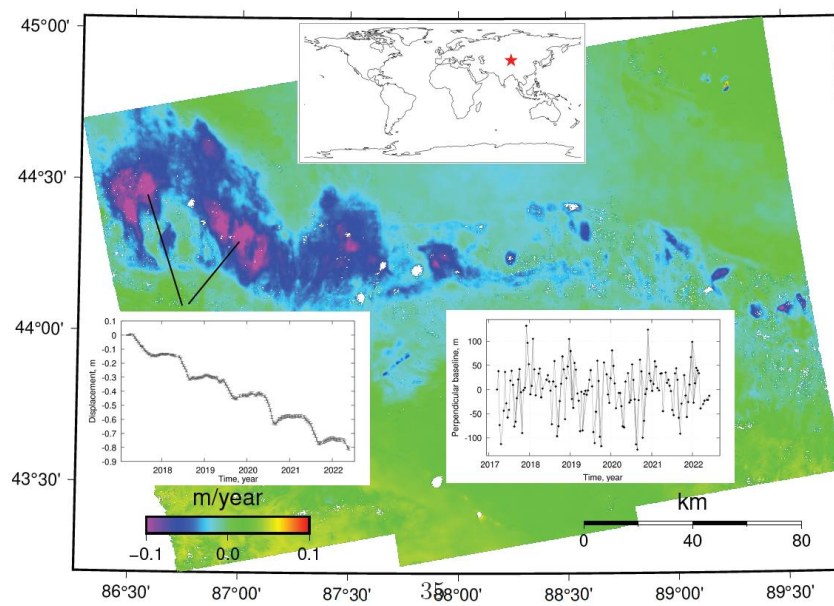
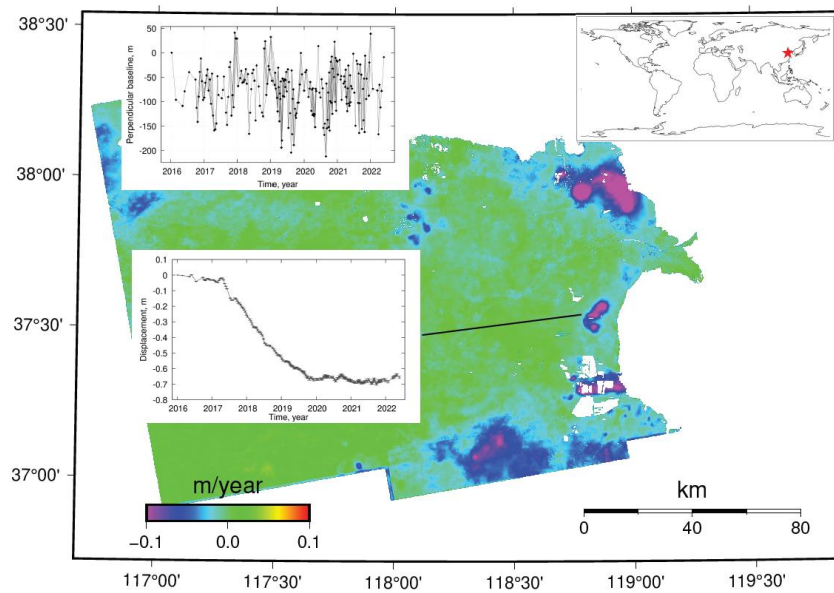
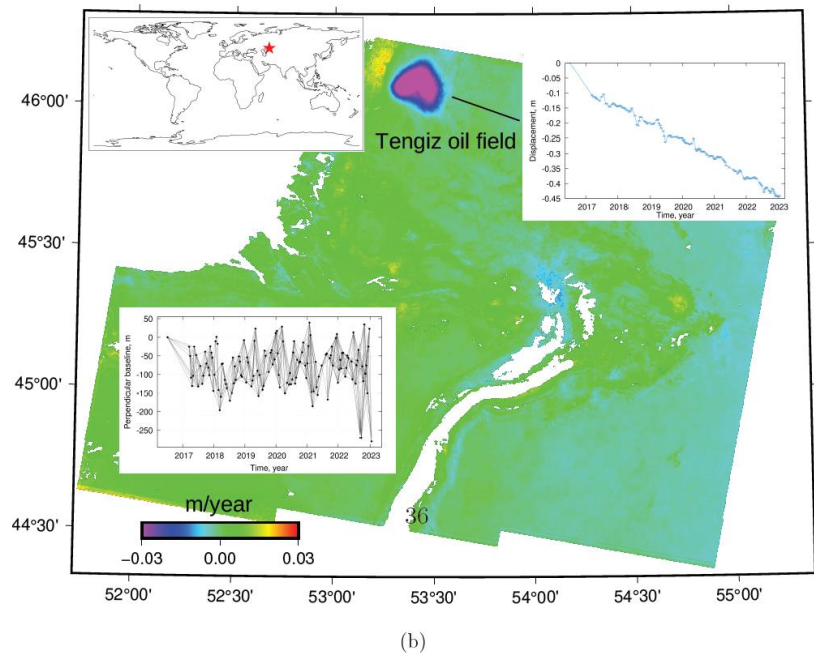
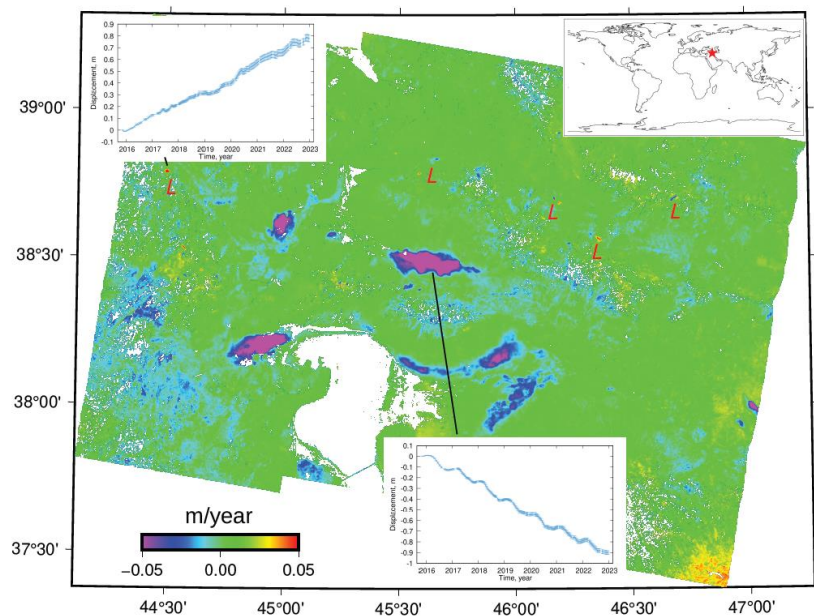


(c)



Canada (super)landslides





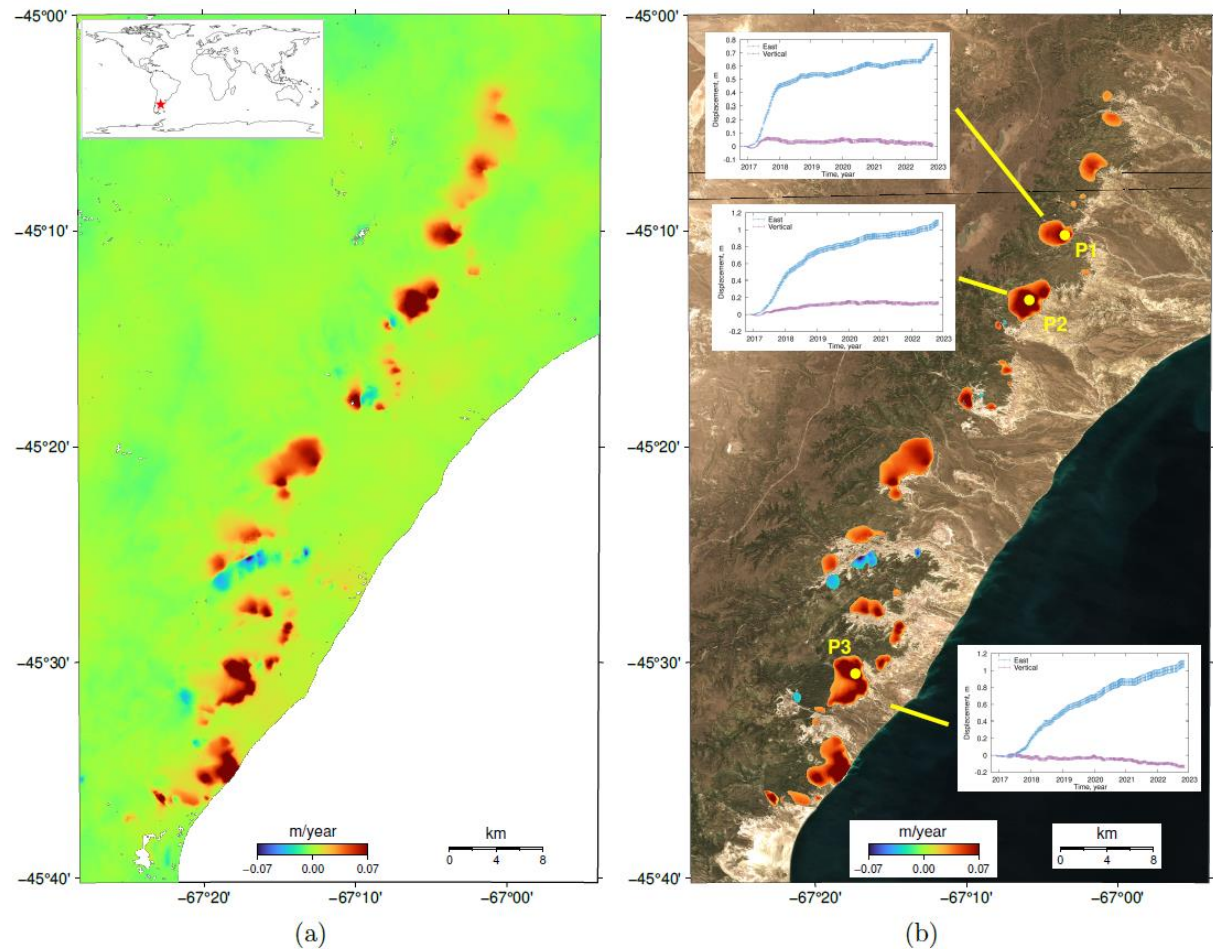


Figure 1: Argentina. (a) Horizontal east deformation rate computed with MSBAS-2D technique from 2017-2023 ascending and descending Sentinel-1 data. Westward deformation is negative, and eastward is positive. (b) Areas with fast deformation rates that are likely slow-moving deep-seated landslides are plotted over Sentinel-2 image. Insets show 2D deformation time series at sites P1-P3.

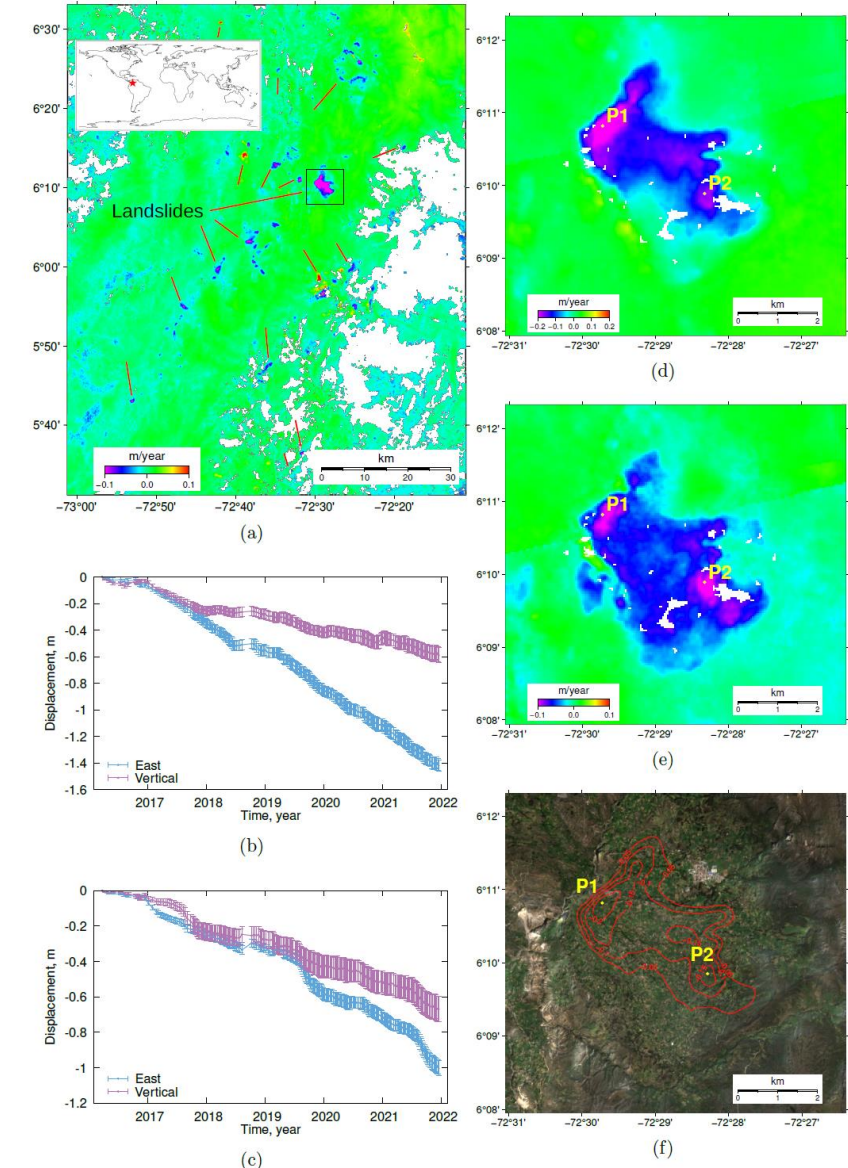


Figure 2: Columbia. Line-of-sight (a) deformation rate computed with MSBAS-1D technique from 2017-2023 descending Sentinel-1 data. Westward deformation and subsidence are negative, and eastward and uplift are positive. Several landslides are marked with red lines. Time series of ground deformation at sites P1 (b) and P2 (c). Horizontal east (d) and vertical (e) deformation rates computed with MSBAS-2D technique from subset (black rectangle in (a)) of ascending and descending Sentinel-1 data. (f) Contour lines of horizontal east rate from (d), in range 0.05-0.20 m/year, are plotted over Sentinel-2 image.

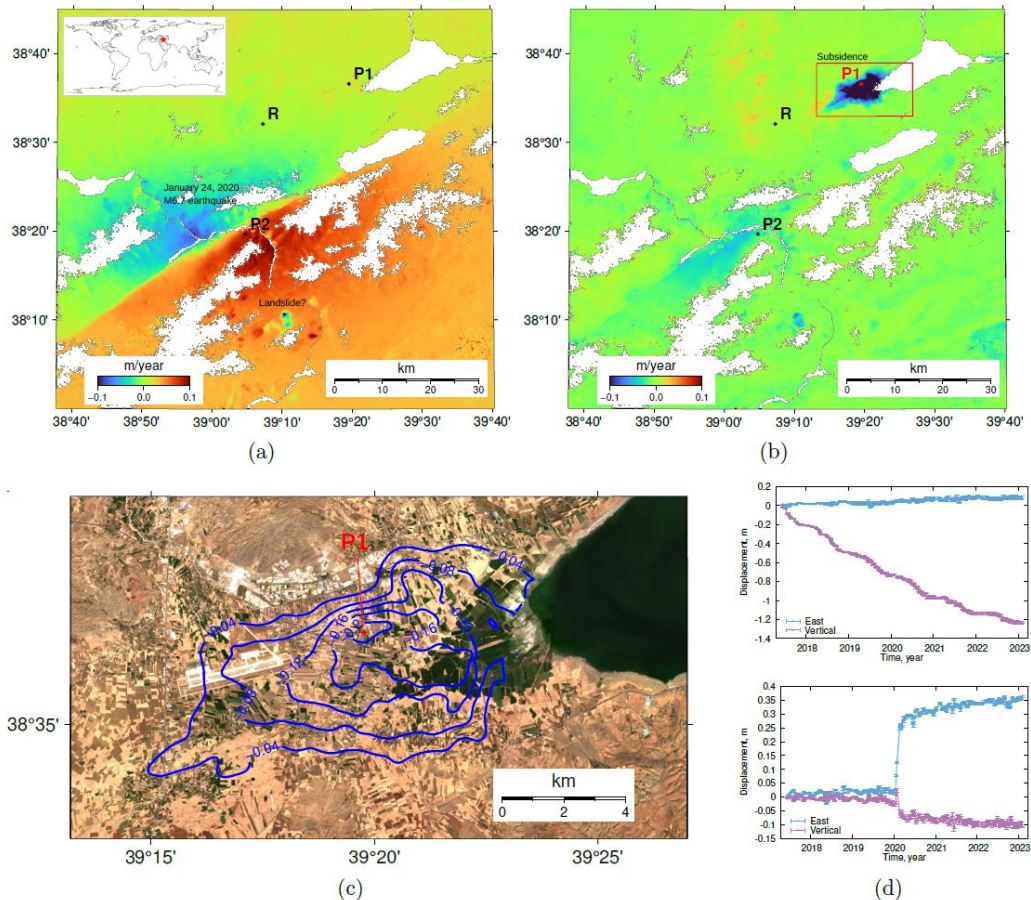


Figure 3: Turkey. Horizontal east (a) and vertical (b) deformation rate computed with MSBAS-2D technique from 2017-2023 ascending and descending Sentinel-1 data relative reference region R. Westward deformation and subsidence are negative, and eastward and uplift are positive. (c) Area experiencing rapid subsidence. Contour lines of subsidence rate from (b), in range 0.04-0.20 m/year, are plotted over Sentinel-2 image. (d-e) Time series of ground deformation at sites P1 (top) and P2 (bottom). Observed horizontal deformation is due to January 24 2020, M6.7 earthquake and landslide. Observed vertical deformation is likely due to extraction of groundwater.

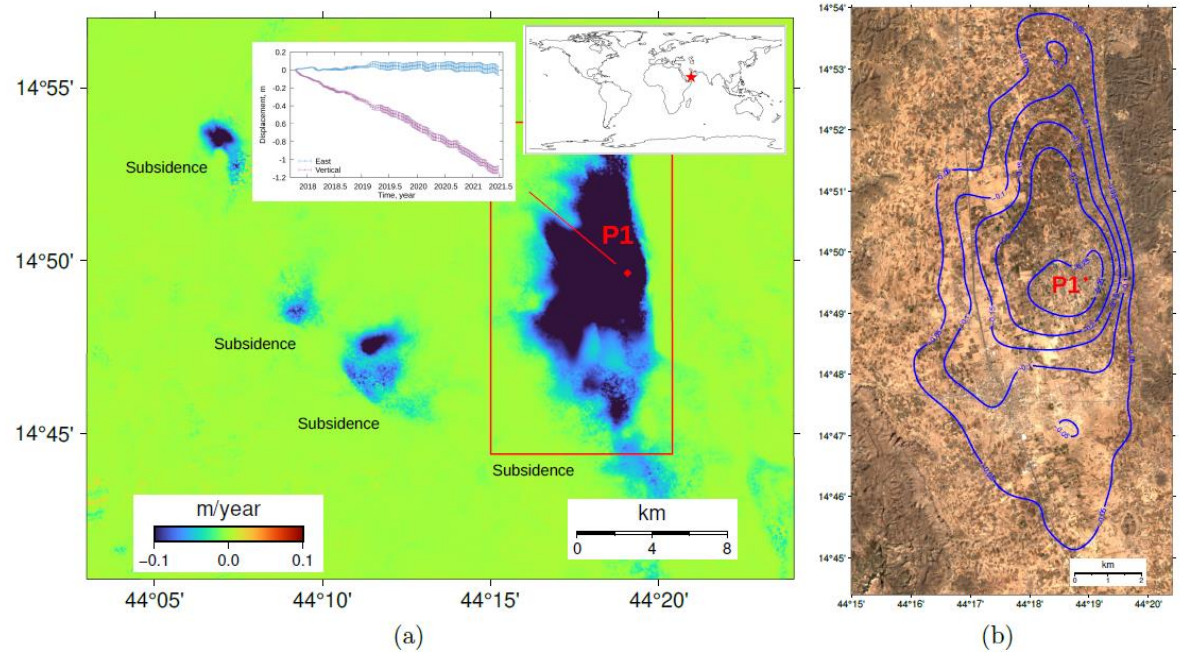


Figure 4: Yemen. (a) Vertical deformation rate computed with MSBAS-2D technique from 2017-2021 ascending and descending Sentinel-1 data. Subsidence is negative. Insert shows deformation time series at site P1. (b) Area experiencing rapid subsidence. Contour lines of subsidence rate from (a), in range 0.05-0.25 m/year, are plotted over Sentinel-2 image.

MSBAS 3D-SPF, 3D, 4D

- Recall

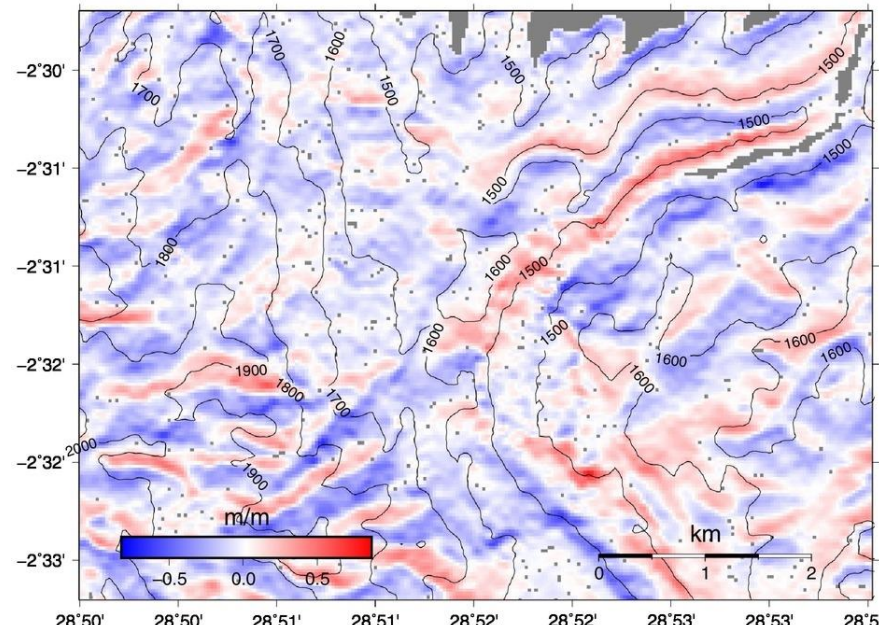
Table 1: Dimension of MSBAS time series is determined by type of input data and control flags. RO_{asc} , RO_{dsc} , AO_{asc} , AO_{dsc} are ascending and descending range and ascending and descending azimuth measurements. DInSAR and SPO-RO range measurements are considered equivalent. More than one set of similar type can be used. DD_NSEW_FILES are first central derivatives along north and east directions. D_FLAG is processing control flag. SPF is Surface-Parallel Flow constraint.

No	MSBAS Technique	RO_{asc}	RO_{dsc}	AO_{asc}	AO_{dsc}	DD_NSEW_FILES	$D_FLAG = 1$
1	1D	×					
2	1D		×				
3	1D			×			
4	1D				×		
5	2D	×	×				
6	3D	×	×	×			
7	3D	×	×		×		
8	3D	×	×	×	×		
9	3D-SPF	×	×			×	
10	3D-SPF	×		×		×	
11	3D-SPF		×		×	×	
12	3D-SPF	×	×	×		×	
13	3D-SPF	×	×		×	×	
14	3D-SPF	×	×	×	×	×	
15	4D	×	×	×		×	×
16	4D	×	×		×	×	×
17	4D	×	×	×	×	×	×

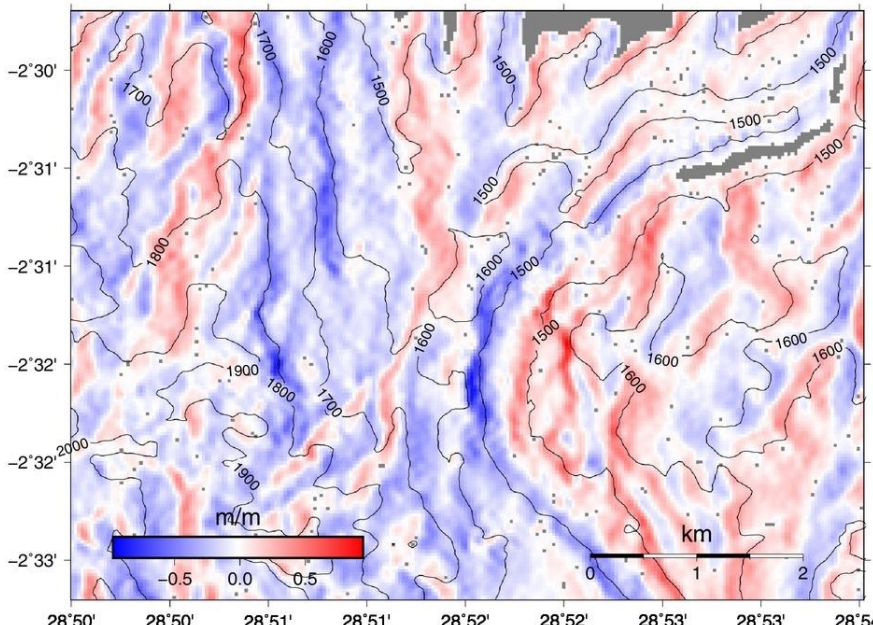
DInSAR == SPO-RO

MSBAS 3D-SPF

- Assumes flow parallel to surface
- DEM first central derivatives along the north and east directions
 - gmt grdfilter dem.tif -D2 -Fg10 -fg -Gdem_flt.tif=gd+n0:Gtiff (i.e., **10 km window**)
 - gmt grdmath dem_flt.tif DDY 0 DENAN -M -fg = dem_flt_ns.tif=gd+n0:Gtiff
 - gmt grdmath dem_flt.tif DDX 0 DENAN -M -fg = dem_flt_ew.tif=gd+n0:Gtiff

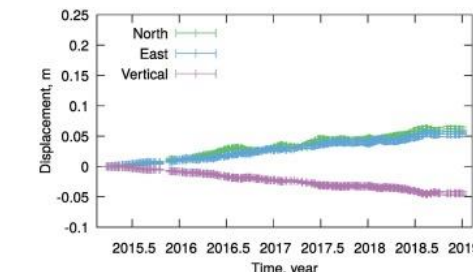
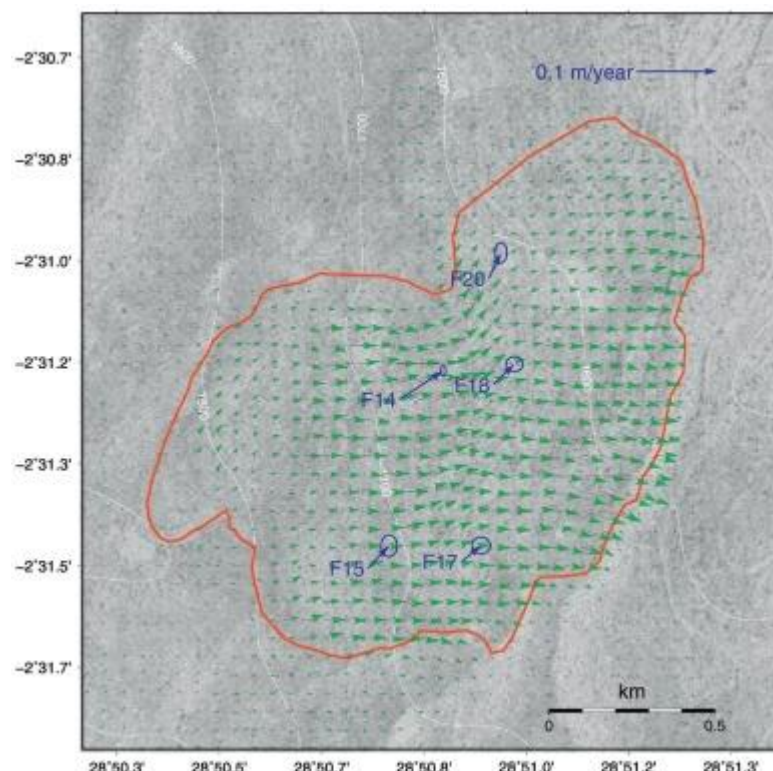
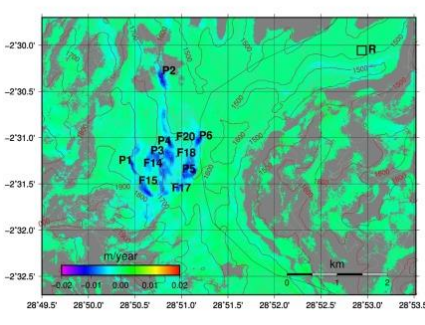
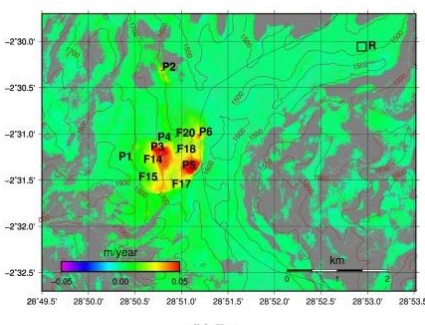
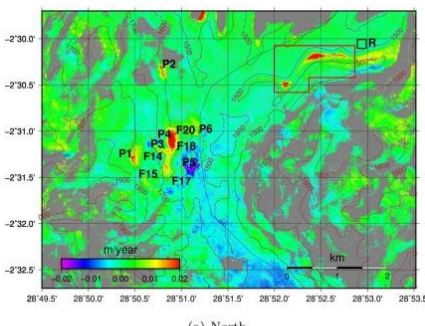


(a) First derivative along north direction

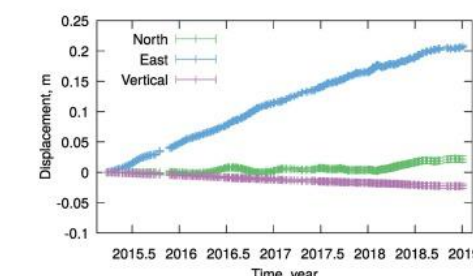


(b) First derivative along east direction

MSBAS 3D-SPF (cont.)

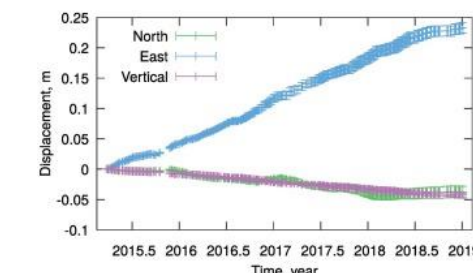


(a) P1

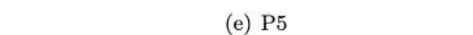


(b) P2

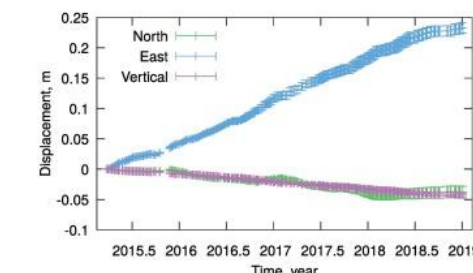
(c) P3



(d) P4



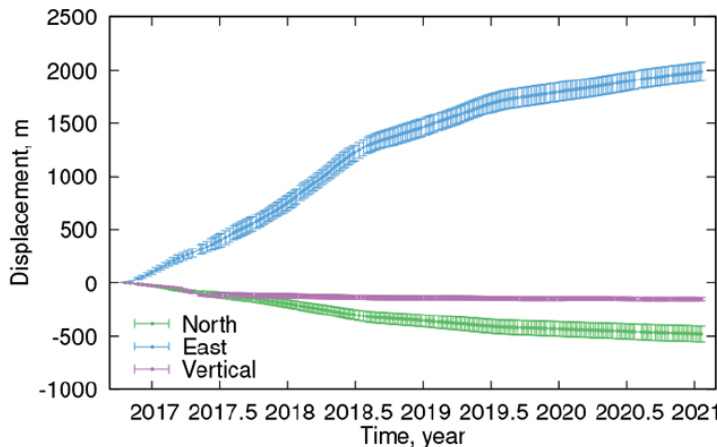
(e) P5



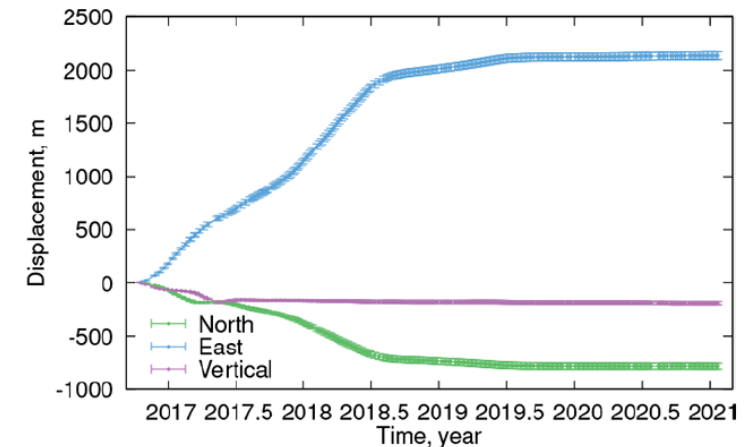
(f) P6

Flow time series

Cumulative flow displacement

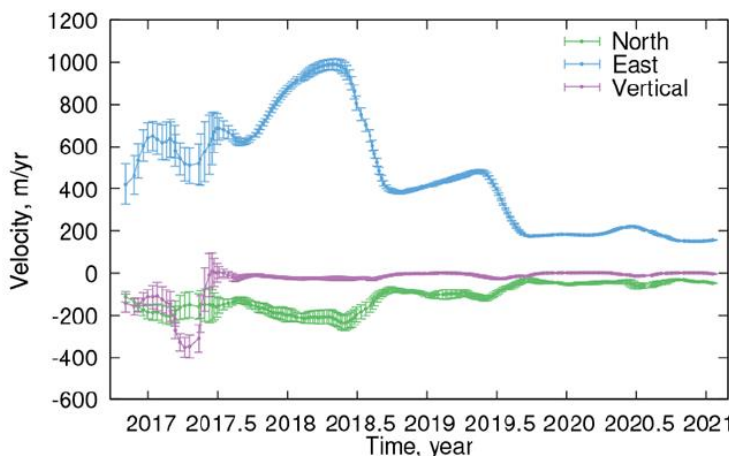


(e) P5

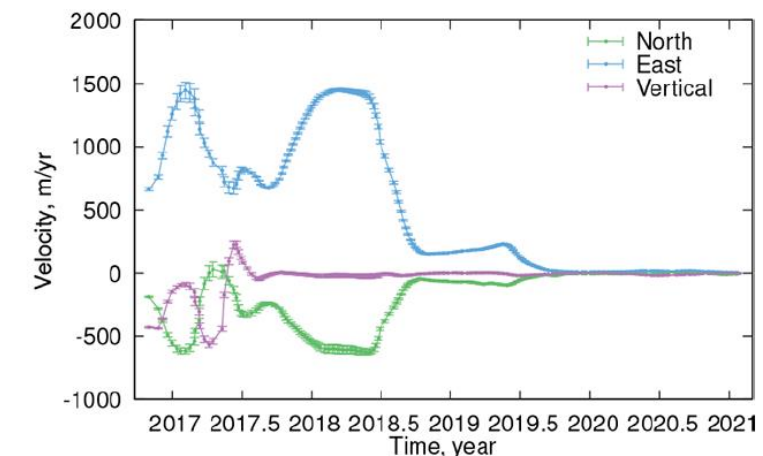


(f) P6

Instantaneous flow rate



(e) P5



(f) P6

MSBAS 3D, requires SPO-AO, no DEM

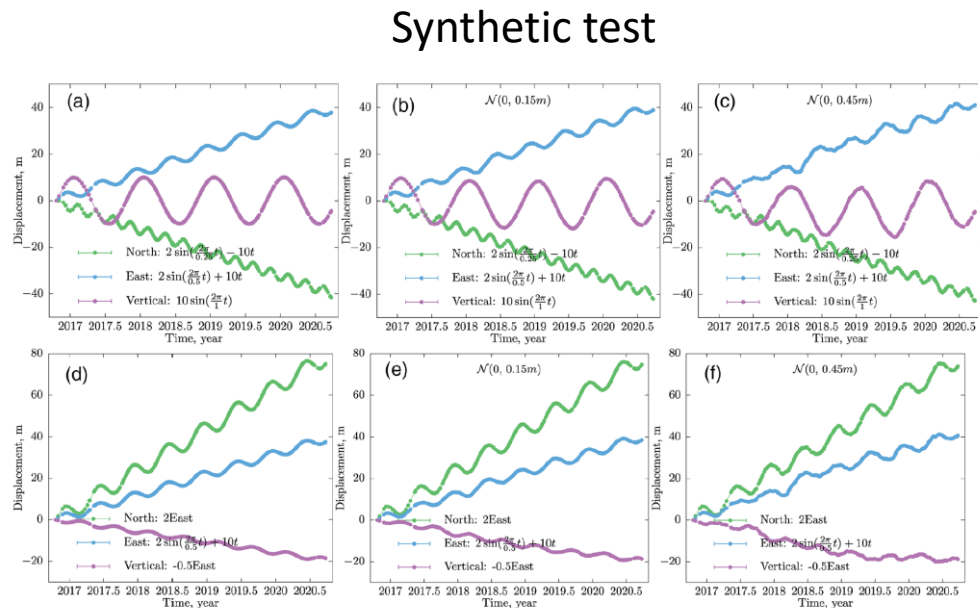


Figure 3. Results of numerical simulations demonstrating the ability of this technique to reconstruct complex uncorrelated and correlated input signals in all three components. Equations of input signals are shown in corresponding subfigure legends; t is time. Harmonic and linear input signals are assumed. Gaussian noise with a mean value of zero and standard deviations in the range 0.15–0.45 m (which is approximately 10%–30 % of the signal) is added to subfigures in the second and third columns.

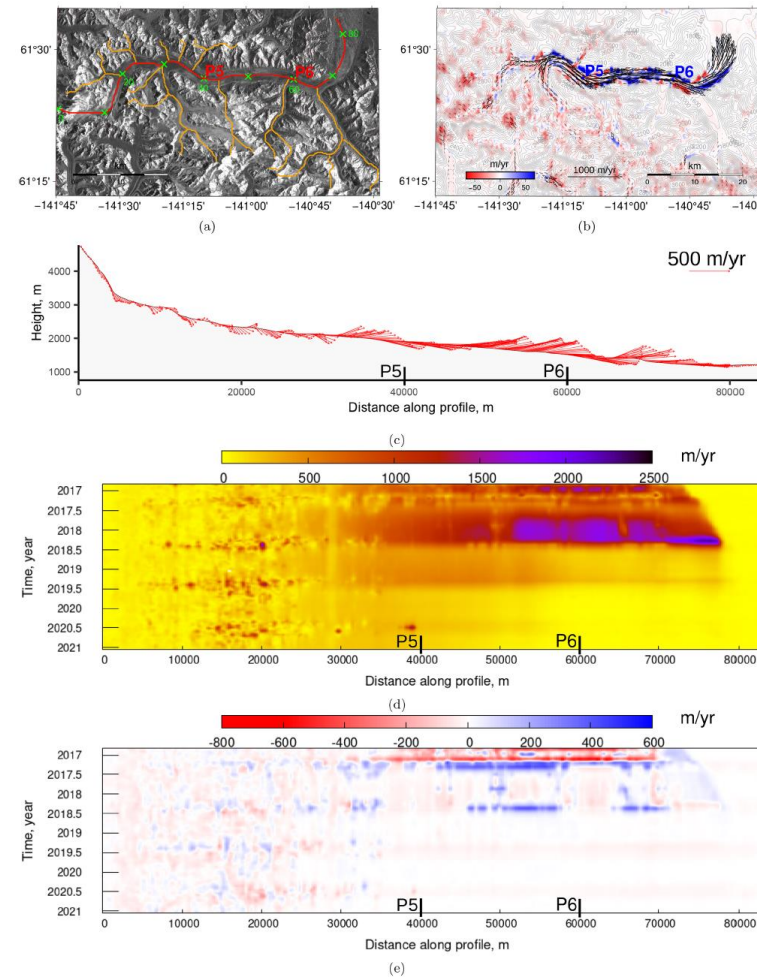


Figure 8. (a) Sentinel-1 SAR intensity image acquired on 22 December 2019 over AOI2 that covers Klutlan Glacier (KtG). Flow lines are in orange and red. Markers in green show the distance in kilometers along the selected red flow line. (b) Time-averaged 3D flow velocities: horizontal velocity is shown as a (coarse-resolution) vector map, and vertical velocity is color-coded. Surface topographic contour lines derived from the TerraSAR-x 90m DEM with intervals of 100m are shown in gray. Flow displacement time series for regions P5–P6 are plotted in Fig. 11. (c) Time-averaged 3D flow velocities and glacier height along the red flow line. (d) Temporal evolution of horizontal flow velocity magnitude along the red flow line. (e) Temporal evolution of vertical flow velocity along the red flow line.

MSBAS 4D

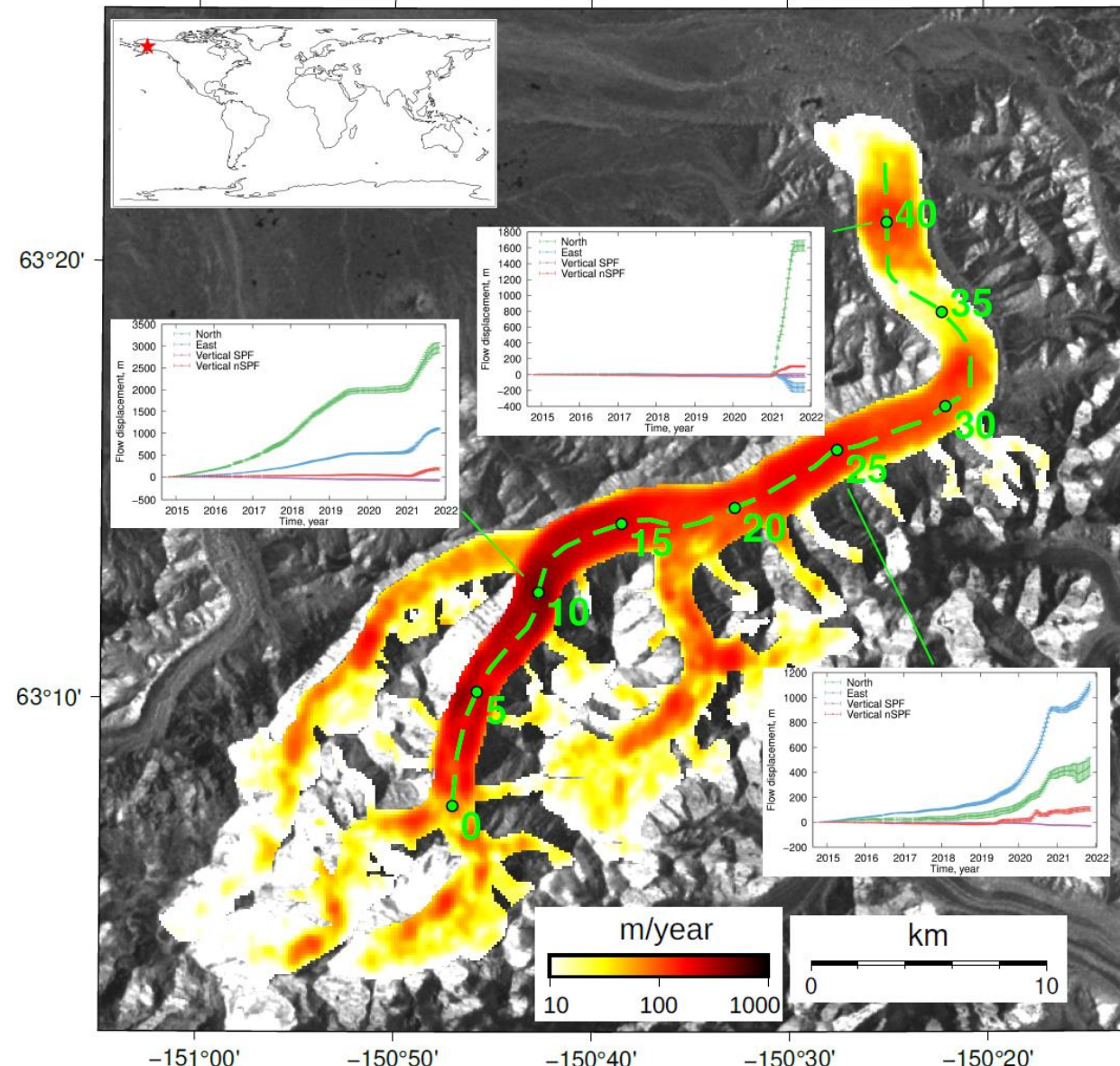


Figure 5: Alaska. Magnitude of flow velocity at Muldrow Glacier computed with MSBAS-4D technique from 2014-2022 ascending and descending Sentinel-1 data. Central flowline and 10 km marks are plotted in green. Inserts show flow velocity time series for sites at 10, 25, and 40 km. Background is Sentinel-1 SAR intensity image. Modified from [8].

References (see Table 2 slide 6)

- [4] S. Samsonov, N. d'Oreye, Multidimensional Small Baseline Subset (MSBAS) for Two-Dimensional Deformation Analysis: Case Study Mexico City, *Can. J. Remote. Sens.* 43 (4) (2017). doi:10.1080/07038992.2017.1344926.
- [5] N. d'Oreye, D. Derauw, S. Samsonov, M. Jaspard, D. Smittarello, *Mas-Ter: A full automatic multi-satellite InSAR mass processing tool for rapid incremental 2D ground deformation time series*, in: 2021 IEEE International Geoscience and Remote Sensing Symposium IGARSS, IEEE, 2021. doi:10.1109/igarss47720.2021.9553615.
- [6] J. P. Dudley, S. V. Samsonov, *The Government of Canada automated processing system for change detection and ground deformation analysis from RADARSAT-2 and RADARSAT Constellation Mission Synthetic Aperture Radar data: description and user guide*, Tech. rep., Geomatics Canada Open File 63 (2020). doi:10.4095/327790.
- [8] S. V. Samsonov, *Operational processing of big satellite data for monitoring glacier dynamics: Case study of Muldrow Glacier*, *Remote Sensing* 14 (11) (2022) 2679. doi:10.3390/rs14112679.
- [9] S. Samsonov, W. Feng, *Preliminary retrievals of deformation rates based on 2017–2023 Sentinel-1 data computed with the MSBAS system*, Mendeley Data, V.3 (2022). doi:10.17632/t7wvtrk28y.3.
- [10] S. Samsonov, *Data for: Estimation of deformation intensity above a flooded potash mine near Berezniki (Perm Krai, Russia) with SAR interferometry* (2020). doi:10.17632/CKC3HGZ2DH.1.
- [11] S. Samsonov, *Data for: SAR-derived flow velocity and its link to glacier surface elevation change and mass balance* (2020). doi:10.17632/9D96C5BDDM.1.
- [12] S. Samsonov, *Data for: Measuring the state and temporal evolution of glaciers in Alaska and Yukon using SAR-derived 3D time series of glacier surface flow* (2021). doi:10.17632/ZF67RSGYDV.1.
- [13] S. Samsonov, N. d'Oreye, B. Smets, *Ground deformation associated with post-mining activity at the French-German border revealed by novel InSAR time series method*, *Int. J. Appl. Earth Obs. Geoinf.* 23 (2013) 142–154. doi:10.1016/j.jag.2012.12.008.
- [14] S. Samsonov, P. Gonzalez, K. Tiampo, N. d'Oreye, *Methodology for spatio-temporal analysis of ground deformation occurring near Rice Lake (Saskatchewan) observed by RADARSAT-2 DInSAR during 2008–2011*, *Can. J. Remote. Sens.* 39 (1) (2013) 27–33.
- [15] S. Samsonov, P. Gonzalez, K. Tiampo, d'Oreye N., *Modeling of fast ground subsidence observed in southern Saskatchewan (Canada) during 2008–2011*, *Nat. Hazards Earth Syst. Sci.* 14 (2014) 247–257. doi:doi:10.5194/nhess-14-247-2014.
- [16] S. Samsonov, A. Baryakh, *Estimation of deformation intensity above a flooded potash mine near Berezniki (Perm Krai, Russia) with SAR interferometry*, *Remote Sensing* 12 (19) (2020) 3215. doi:10.3390/rs12193215.
- [17] J. Pearse, V. Singhroy, S. Samsonov, J. Li, *Anomalous surface heave induced by enhanced oil recovery in northern Alberta: InSAR observations and numerical modeling*, *Journal of Geophysical Research* (2014). doi:10.1002/2013JB010885.
- [18] S. Samsonov, *Short- and long-term ground deformation due to cyclic steam stimulation in Alberta, Canada, measured with interferometric radar*, *Leading Edge* 36 (1) (2017) 36–42. doi:10.1190/tle36010036.1.
- [19] S. Samsonov, K. Tiampo, W. Feng, *Fast subsidence in downtown of Seattle observed with satellite radar*, *Remote Sens. Appl.: Soc. Environ.* 4 (2016) 179–187. doi:10.1016/j.rsase.2016.10.001.
- [20] S. Samsonov, N. d'Oreye, P. Gon'alez, K. Tiampo, L. Ertolahti, J. Clague, *Rapidly accelerating subsidence in the Greater Vancouver region from two decades of ERS-ENVISAT-RADARSAT-2 DInSAR measurements*, *Remote Sens. Environ.* 143 (5) (2014) 180–191. doi:10.1016/j.rse.2013.12.017.
- [21] S. V. Samsonov, T. C. Lantz, S. V. Kokelj, Y. Zhang, *Growth of a young pingo in the Canadian Arctic observed by RADARSAT-2 interferometric satellite radar*, *The Cryosphere* 10 (2) (2016) 799–810. doi:10.5194/tc-10-799-2016.
- [22] S. Samsonov, K. Tiampo, R. Cassotto, *Measuring the state and temporal evolution of glaciers in Alaska and Yukon using synthetic-aperture-radar-derived (SAR-derived) 3D time series of glacier surface flow*, *The Cryosphere* 15 (9) (2021) 4221–4239. doi:10.5194/tc-15-4221-2021.
- [23] S. Samsonov, *Three-dimensional deformation time series of glacier motion from multiple-aperture DInSAR observation*, *J. Geod.* 93 (2019) 2651–2660. doi:10.1007/s00190-019-01325-y.
- [24] S. Samsonov, K. Tiampo, R. Cassotto, *SAR-derived flow velocity and its link to glacier surface elevation change and mass balance*, *Remote Sens. Environ.* 258 (2021) 112343. doi:10.1016/j.rse.2021.112343.
- [25] S. Samsonov, A. Dille, O. Dewitte, F. Kervyn, N. d'Oreye, *Satellite interferometry for mapping surface deformation time series in one, two and three dimensions: A new method illustrated on a slow-moving landslide*, *Eng. Geol.* 266 (2020) 105471. doi:10.1016/j.enggeo.2019.105471.
- [26] A. Dille, F. Kervyn, A. L. Handwerger, N. d'Oreye, D. Derauw, T. M. Bibentyo, S. Samsonov, J.-P. Malet, M. Kervyn, O. Dewitte, *When image correlation is needed: Unravelling the complex dynamics of a slow-moving landslide in the tropics with dense radar and optical time series*, *Remote Sens. Environ.* 258 (2021) 112402. doi:10.1016/j.rse.2021.112402.
- [27] A. Dille, O. Dewitte, A. L. Handwerger, N. d'Oreye, D. Derauw, G. G. Bamulezi, G. I. Mawe, C. Michellier, J. Moeyersons, E. Monsieurs, T. M. Bibentyo, S. Samsonov, B. Smets, M. Kervyn, F. Kervyn, *Acceleration of a large deep-seated tropical landslide due to urbanization feedbacks*, *Nat. Geosci.* 15 (12) (2022) 1048–1055. doi:10.1038/s41561-022-01073-3.
- [28] S. Samsonov, A. Blais-Stevens, *Satellite interferometry for regional assessment of landslide hazard to pipelines in northeastern British Columbia, Canada*, *Int. J. Appl. Earth Obs. Geoinf.* 118 (2023) 103273. doi:10.1016/j.jag.2023.103273.
- [29] S. V. Samsonov, K. F. Tiampo, A. G. Camacho, J. Fernández, P. J. Gon'alez, *Spatiotemporal analysis and interpretation of 1993–2013 ground deformation at Campi Flegrei, Italy, observed by advanced DInSAR*, *Geophys. Res. Lett.* 41 (17) (2014) 6101–6108. doi:10.1002/2014GL060595.
- [30] S. Samsonov, W. Feng, P. Peltier, H. Geirsson, N. d'Oreye, K. Tiampo, *Multidimensional small baseline subset (MSBAS) for volcano monitoring in two dimensions: opportunities and challenges. Case study Piton de la Fournaise volcano*, *J. Volcanol. Geotherm. Res.* (2016).
- [31] A. G. Camacho, J. Fernández, S. V. Samsonov, K. F. Tiampo, M. Palano, *3D multi-source model of elastic volcanic ground deformation*, *Earth Planet. Sci. Lett.* 547 (2020) 116445. doi:10.1016/j.epsl.2020.116445.
- [32] P. Lundgren, T. Girona, M. G. Bato, V. J. Realmuto, S. Samsonov, C. Cardona, L. Franco, E. Gurrola, M. Aivazis, *The dynamics of large silicic systems from satellite remote sensing observations: the intriguing case of Domuyo volcano, Argentina*, *Sci. Rep.* 10 (1) (jul 2020). doi:10.1038/s41598-020-67982-8.
- [33] D. Derauw, d'Oreye Nicolas, M. Jaspard, A. Caselli, S. Samsonov, *Ongoing automated ground deformation monitoring of Domuyo - Laguna del Maule area (Argentina) using Sentinel-1 MSBAS time series: Methodology description and first observations for the period 2015–2020*, *J. South Amer. Earth Sci.* 104 (2020) 102850. doi:10.1016/j.jsames.2020.102850.
- [34] S. Samsonov, M. Czarnogorska, D. White, *Satellite interferometry for highprecision detection of ground deformation at a carbon dioxide storage site*, *Int. J. Greenhouse Gas Control* 42 (2015) 188–199. doi:doi:10.1016/j.ijggc.2015.07.034.
- [35] M. Czarnogorska, S. Samsonov, D. White, *Airborne and spaceborne remote sensing characterization for Aquistore carbon capture and storage site*, *Can. J. Remote. Sens.* 42 (2016) 274–290. doi:10.1080/07038992.2016.1171131.
- [36] D. W. Vasco, T. H. Dixon, A. Ferretti, S. V. Samsonov, *Monitoring the fate of injected CO₂ using geodetic techniques*, *The Leading Edge* 39 (1) (2020) 29–37. doi:10.1190/tle39010029.1.
- [37] S. V. Samsonov, W. Feng, Y. Fialko, *Subsidence at Cerro Prieto Geothermal Field and postseismic slip along the indusivo fault from 2011 to 2016 RADARSAT-2 DInSAR time series analysis*, *Geophys. Res. Lett.* 44 (6) (2017) 2716–2724. doi:10.1002/2017gl072690.
- [38] D. W. Vasco, J. Rutqvist, P. Jeanne, S. V. Samsonov, C. Hartline, *Using geodetic data in geothermal areas*, *The Leading Edge* 39 (12) (2020) 883–892. doi:10.1190/tle39120883.1.
- [39] D. W. Vasco, S. V. Samsonov, K. Wang, R. Burgmann, P. Jeanne, W. Foxall, Y. Zhang, *Monitoring natural gas storage using synthetic aperture radar: are the residuals informative?*, *Geophys. J. Int.* 228 (2) (2021) 1438–1456. doi:10.1093/gji/ggab409.
- [40] S. V. Samsonov, A. P. Trishchenko, K. Tiampo, P. J. Gon'alez, Y. Zhang, J. Fernández, *Removal of systematic seasonal atmospheric signal from interferometric synthetic aperture radar ground deformation time series*, *Geophys. Res. Lett.* 41 (17) (2014) 6123–6130. doi:10.1002/2014GL061307.